

Measurement of many-body chaos using a quantum clock

Guanyu Zhu,¹ Mohammad Hafezi,^{1,2,3} and Tarun Grover^{4,2}

¹*Joint Quantum Institute, NIST–University of Maryland, College Park, Maryland 20742, USA*

²*Kavli Institute of Theoretical Physics, Santa Barbara, California 93106, USA*

³*Department of Electrical and Computer Engineering and Institute for Research in Electronics and Applied Physics, University of Maryland, College Park, Maryland 20742, USA*

⁴*Department of Physics, University of California, San Diego, La Jolla, California 92093, USA*

(Received 12 August 2016; published 22 December 2016)

There has been recent progress in understanding chaotic features in many-body quantum systems. Motivated by the scrambling of information in black holes, it has been suggested that the time dependence of out-of-time-ordered (OTO) correlation functions such as $\langle O_2(t)O_1(0)O_2(t)O_1(0) \rangle$ is a faithful measure of quantum chaos. Experimentally, these correlators are challenging to access since they apparently require access to both forward and backward time evolution with the system Hamiltonian. Here we propose a protocol to measure such OTO correlators using an ancilla that controls the direction of time. Specifically, by coupling the state of the ancilla to the system Hamiltonian of interest, we can emulate the forward and backward time propagation, where the ancilla plays the role of a quantum clock. Within this scheme, the continuous evolution of the entire system (the system of interest and the ancilla) is governed by a time-independent Hamiltonian. We discuss the implementation of our protocol with current circuit-QED technology for a class of interacting Hamiltonians. Our protocol is immune to errors that could occur when the direction of time evolution is externally controlled by a classical switch.

DOI: [10.1103/PhysRevA.94.062329](https://doi.org/10.1103/PhysRevA.94.062329)

I. INTRODUCTION

Characterizing chaos in single-particle quantum systems is an old and rich topic with roots in semiclassical quantization [1]. However, there is less understanding of chaos in many-body quantum systems and quantum field theories, especially away from the semiclassical limit. Recently, progress has been obtained in characterizing chaos in quantum many-body systems using insights from the scrambling of information in black holes [2–4]. Specifically, it has been argued that under certain assumptions, the time dependence of the four-point correlation function $\langle O_2(t)O_1(0)O_2(t)O_1(0) \rangle$ involving any two local operators O_1 and O_2 is a measure of quantum chaos, where the angular brackets denote averaging over a canonical ensemble.¹ Since this correlator is the overlap between two states that are obtained by applying the noncommuting operators $O_1(0)$ and $O_2(0)$ in reverse order with respect to each other, the basic intuition is that it captures the sensitivity of the evolved system to initial conditions.² Remarkably, it has been shown by Maldacena *et al.* [4] that such a correlator cannot grow faster than $e^{\lambda t}$, with a universal bound $\lambda \leq 2\pi T/\hbar$, thus defining a maximal Lyapunov exponent. Even more, the bound is known to be saturated by certain large- N conformal field theories that are holographically described by Einstein’s gravity [2,6,7] and also [8,9] by a nonlocal Hamiltonian [the Sachdev-Ye-Kitaev (SYK) model], originally discussed by Sachdev and Ye [10] and more recently in the context of holography by Sachdev [11] and Kitaev [3].

The peculiar feature of the correlator $\langle O_2(t)O_1(0)O_2(t)O_1(0) \rangle$ is that it is not time ordered

and thus, from an experimental point of view, requires access to time evolution by Hamiltonians H and $-H$. Recently, an interesting proposal was made in Ref. [12] where Sachdev and Ye outlined a protocol to measure $\langle O_2(t)O_1(0)O_2(t)O_1(0) \rangle$. The sign of the Hamiltonian in Ref. [12] is changed via a classical switch by noticing that the sign of interactions in a cavity QED depends on the sign of the two-photon detuning. However, any imperfection in this sign reversal due to experimental imperfections could lead to significant error in out-of-time-ordered (OTO) correlators.

In this paper we address this issue by proposing a quantum clock to control the sign of a certain many-body Hamiltonian and use it to construct a proposal to measure OTO correlators such as $\langle O_2(t)O_1(0)O_2(t)O_1(0) \rangle$. The basic idea is to couple the Hamiltonian H of interest to an ancilla qubit $\bar{\tau}$ linearly such that $H_{\text{tot}} = \tau^z \otimes H$ and then perform a unitary time evolution of the state $(|\uparrow\rangle + |\downarrow\rangle) \otimes |\psi\rangle_S$, where $|\psi\rangle_S$ is some initial state of the system of interest. By construction of H_{tot} , the $|\uparrow\rangle$ branch of the wave function effectively evolves forward in time while the $|\downarrow\rangle$ branch evolves backward. Therefore, the ancilla qubit $\bar{\tau}$ effectively acts like a quantum clock that controls the direction of time evolution. The OTO correlator $\langle O_2(t)O_1(0)O_2(t)O_1(0) \rangle$ is then measured by conditionally applying different operators on the forward and backward evolving branches of the wave function and finally measuring the expectation value of the operator τ^x acting on the quantum clock.

From an experimental standpoint, our protocol is motivated by the rapid development of quantum simulation and information technology in recent years, such as cavity quantum electrodynamics (QED) [13–16], circuit-QED [17–28], Rydberg atoms [29–32], and trapped ions [33]; it is within current technology to engineer an ancilla qubit coupled to a many-body system globally. The ancilla qubit can be either the cavity photon mode or the internal state of an atom. The mechanism of the coupling is usually through dispersive interaction, which can originate, for example, from Jaynes-Cummings interaction

¹Although the relation between such correlators and semiclassical chaos was first observed a while ago [5], it is only recently that progress has been made in more general settings.

²If O_1 and O_2 were canonically conjugate, then semiclassically this correlator is indeed given by $(\frac{dO_2(t)}{dO_2(0)})^2$, which is the canonical way to define sensitivity of time evolution to the initial conditions.

[34] perturbatively [14,18,35] or from the Rydberg blockade mechanism [30,36–38]. Such an ancilla has been widely used as a controlled-phase gate [30,35–38] for quantum information processing and quantum simulation [39] and has been used to measure time-ordered correlation functions [40]. Meanwhile, theoretical proposals suggest that such an ancilla can be used as a quantum switch that performs a many-body Ramsey interferometer [41,42] to extract useful information of the quantum system, such as entanglement entropy [43] and the spectrum [44]. In this paper the ancilla, in addition to playing the role of the quantum clock, has the added benefit of being the probe of the system. Specifically, we show how the OTO correlator could be obtained by measuring the same ancilla.

The primary advantage of our protocol utilizing a quantum clock for both control and readout of the many-body states is its robustness against statistical errors, such as imperfect rotation, in each shot of the experiments. In particular, our protocol involves only one copy of the many-body system and our quantum clock does not modify the many-body Hamiltonian during the protocol, which is in contrast to a previous proposal of measuring the same correlator using a classical switch to change the sign of the Hamiltonian [12] and a recent proposal using two copies of many-body systems [45]. Our protocol is less sensitive to the potential errors that can make the forward and backward propagation asymmetric in the protocol of [12] or errors that may lead to nonidentical copies in the protocol of Ref. [45]. These errors can make extracting the functional dependence of the OTO correlator, including extracting physical quantities such as the Lyapunov exponent or the butterfly velocity (the velocity of ballistic growth of local operators) [46,47], challenging. In addition, we are also able to construct a local Hamiltonian, which is more physical from condensed-matter and quantum-field-theoretic viewpoints and may also exhibit a richer behavior of quantum chaos, such as the recent discovery of the power-law scrambling in many-body localized systems [48–52], and faster scrambling near quantum phase transitions of a Bose-Hubbard model [53].

We also provide simple examples of embedding such an ancilla in cavity-QED systems for both a nonlocal all-to-all coupled spin models and a local XY -spin or extended Bose-Hubbard model. In the nonlocal model, qubits (spins) are interacting with each other mediated by a passive cavity bus, which is itself dispersively coupled to another ancilla cavity in order to control the sign of the Hamiltonian. To realize the local model, local cavities or resonators are coupled by intermediate qubits, which are themselves coupled to a global cavity. When integrating out the qubit degrees of freedom and with proper choice of parameters, the effective Hamiltonian has an overall sign controlled by the state of the global cavity. Such models can be realized with recently developed experimental platforms such as the circuit-QED network [19–22,24,25,54] and a qubit or atomic array in a three-dimensional (3D) cavity [26,27].

The outline of our paper is as follows. In Sec. II we present our general protocol of measuring the OTO correlator with a quantum clock. In Sec. III we show how such a quantum clock could be embedded in a physical model. In Sec. IV we discuss the implementation of the protocol with circuit-QED systems. In Sec. V we analyze the stability of our protocol against imperfections. We present a generalization

of the approach for the extended Bose-Hubbard model and disordered spin chains in Sec. VI. We provide a summary and outlook in Sec. VII. We show details of the experimental realization of the local model, which we construct in the main text with a circuit-QED network or a qubit array in a 3D cavity, in Appendix A. In Appendix B we compare the numerical diagonalization of the original and second-order effective Hamiltonian. Finally, in Appendix C we provide a complete formula of the second-order dispersive Hamiltonian we mention in Sec. III without integrating out the qubits.

II. GENERAL SCHEME

We consider a many-body system governed by Hamiltonian H and couple it globally to an ancilla qubit τ^z , with the total Hamiltonian being

$$H_{\text{tot}} = \tau^z \otimes H. \quad (1)$$

With the cavity-QED implementation, the ancilla qubit can also be realized with the global cavity photon mode as $\tau^z = 1 - 2a^\dagger a$, if the cavity photon state is restricted in the zero- and one-photon subspace. Hence the total Hamiltonian of the coupled system can also be expressed as

$$H_{\text{tot}} = (1 - 2a^\dagger a) \otimes H. \quad (2)$$

From now on, we call both the cavity and the ancilla qubit a clock without further specification, since they play the same role as our quantum clock and one can use either of them for the protocol.

In Eqs. (1) and (2) the clock only dresses the many-body system H and does not exchange excitations (photons) with the many-body system. Crucially, if the H we consider is a local Hamiltonian, the clock does not mediate long-range interaction between the particles or spins in the many-body system and preserves the locality of H .

The only thing that the clock does is control the overall sign of the many-body Hamiltonian H quantum coherently. If the cavity contains no photon, namely, the clock is in state $|0_a\rangle$,³ the overall sign is positive; if the cavity contains one photon, namely, the clock is in state $|1_a\rangle$, the overall sign is negative. If we consider the dynamics of the coupled system, we can express the evolution operator as

$$U_{\text{tot}}(t) = e^{-iH_{\text{tot}}t} = e^{-iHt} \otimes |0_a\rangle\langle 0_a| + e^{iHt} \otimes |1_a\rangle\langle 1_a|. \quad (3)$$

This means that the many-body system H evolves forward in time if the cavity contains no photon and backward in time if the cavity contains one photon. Namely, the cavity photon number $a^\dagger a$ or the ancilla qubit τ^z acts a binary quantum clock that controls the arrow of time. More interestingly, since the clock is a quantum degree of freedom, the system can be in a parallel superposition of evolving both forward and backward in time, for example, when we prepare the clock in the superposition state $\frac{1}{\sqrt{2}}(|0_a\rangle + |1_a\rangle)$.

Now we discuss a general protocol to measure the OTO correlator $\langle O_2(t)O_1(0)O_2(t)O_1(0) \rangle$ introduced earlier, where

³In our convention, the ancilla state $|0_a\rangle$ corresponds to the $|\uparrow\rangle$ spin state.

O_1 and O_2 are certain operators and $O(t) = e^{iHt} O e^{-iHt}$ is the Heisenberg evolved operator. The average could be with respect to a certain initial state $|\psi\rangle_S$ or an ensemble average over a thermal density matrix $\rho_S = \sum_S \frac{e^{-\beta H}}{Z} |\psi\rangle_S \langle\psi|$, where Z is the partition function. For the sake of convenience, we will focus on averaging with respect to a given pure state $|\psi\rangle_S$. If one is interested in averaging with respect to a thermal ensemble, one can still work with a pure state that is obtained by time evolving an initial finite-energy density pure state with respect to H [55]. Assuming that the system is generic (nonintegrable), the pure state average is then expected to match the thermal ensemble average at a temperature determined by the energy density of the state [55–57].

In the Schrödinger picture, the correlator corresponding to a particular initial state can be written as

$${}_S \langle \psi | e^{iHt} O_2 e^{-iHt} O_1 e^{iHt} O_2 e^{-iHt} O_1 | \psi \rangle_S.$$

To measure this correlator, we apply the following Ramsey interferometry protocol as illustrated in Fig. 1.

(i) Start with the many-body system in the state $|\psi\rangle_S$ with respect to which we wish to measure the OTO correlator. Thus, the coupled system can be expressed as $|\psi\rangle_S \otimes |0_a\rangle$.

(ii) Apply a Hadamard gate, i.e., a $\pi/2$ rotation (pulse) around the y axis to the clock state: The coupled system is thus prepared in the superposed state $\frac{1}{\sqrt{2}} |\psi\rangle_S \otimes [|0_a\rangle + |1_a\rangle]$. From now on, the evolution of the many-body system is split into two branches, conditioned by the clock state $|0_a\rangle$ and $|1_a\rangle$, respectively.

(iii) Apply a conditional operation

$$C_{O_1,1} = O_1 \otimes |1_a\rangle \langle 1_a| + \mathbb{I}_S \otimes |0_a\rangle \langle 0_a| \quad (4)$$

so that O_1 is applied only to the lower branch of the interferometer conditioned by the clock state $|1_a\rangle$. The coupled system forms an entangled state

$$\frac{1}{\sqrt{2}} [O_1 |\psi\rangle_S \otimes |1_a\rangle + |\psi\rangle_S \otimes |0_a\rangle].$$

(iv) Let the system evolve with the total Hamiltonian H_{tot} for time t according to $U_{\text{tot}}(t)$ represented in Eq. (3). The coupled system is now in an entangled state of evolving forward and backward in time conditioned by the photon number, namely,

$$\frac{1}{\sqrt{2}} [e^{-iHt} O_1 |\psi\rangle_S \otimes |1_a\rangle + e^{iHt} |\psi\rangle_S \otimes |0_a\rangle]. \quad (5)$$

(v) Apply a conditional O_2 on the lower ($|1_a\rangle$) branch

$$C_{O_2,1} = O_2 \otimes |1_a\rangle \langle 1_a| + \mathbb{I}_S \otimes |0_a\rangle \langle 0_a|. \quad (6)$$

(vi) In order to reverse the arrow of time in both branches, we simply apply a τ^x operator (π pulse around the x axis) to flip the clock. Then we let the coupled system evolve for a period of $2t$ and reach the state

$$\frac{1}{\sqrt{2}} [e^{2iHt} O_2 e^{-iHt} O_1 |\psi\rangle_S \otimes |0_a\rangle + e^{-2iHt} e^{iHt} |\psi\rangle_S \otimes |1_a\rangle].$$

(vii) Perform the previous steps (iii)–(vi) in reversal order (with conditioned operations on the other branch) as shown in Fig. 1(a). The coupled system ends up with the final state

$$|\Psi_f\rangle = \frac{1}{\sqrt{2}} [|R\rangle \otimes |1_a\rangle + |L\rangle \otimes |0_a\rangle], \quad (7)$$

where we have abbreviated the wave functions in two branches as

$$|R\rangle \equiv e^{iHt} O_2 e^{-iHt} O_1 |\psi\rangle_S, \quad |L\rangle \equiv O_1 e^{iHt} O_2 e^{-iHt} |\psi\rangle_S.$$

(viii) Measure the expectation value of τ^x operator under the final state $|\Psi_f\rangle$, which effectively takes an overlap between the many-body states in the two branches of the interferometer and leads to

$$\begin{aligned} \langle \tau^x \rangle_f &\equiv \langle \Psi_f | \mathbb{I}_S \otimes \tau^x | \Psi_f \rangle = \text{Re}[\langle L | R \rangle] \\ &= \text{Re}[_S \langle \psi | e^{iHt} O_2 e^{-iHt} O_1 e^{iHt} O_2 e^{-iHt} O_1 | \psi \rangle_S]. \end{aligned} \quad (8)$$

The outcome is the real part of the OTO correlator. Similarly, one can extract the imaginary part by measuring τ^y , since $\langle \tau^y \rangle_f = \text{Im}[\langle L | R \rangle]$.

Note that a part of forward time evolution has been canceled with backward time evolution in both branches [as illustrated in Fig. 1(a) by red dashed lines]. The preparation of states $|R\rangle$ and $|L\rangle$ can be interpreted as two gedanken experiments: (I) apply O_1 , wait for time t , apply O_2 , and go backward in time for $-t$ and (II) apply O_2 at time t , go backward in time for $-t$, and apply O_1 (at an earlier time than applying O_2). The OTO correlator takes the overlap between these two states and hence compares the sensitivity of the state to the order of applying O_1 and $O_2(t)$, or equivalently the sensitivity to the initial condition, and hence characterizes the butterfly effect.

III. PHYSICAL MODELS

In this section we present physical models with a generic cavity-QED array implementation, which can be realized with, e.g., a circuit-QED network and a superconducting qubit array in a 3D cavity. More experimental details of the realization will be discussed in the next section. The central idea here is to use an ancilla cavity (quantum clock), which enables both quantum switching of the arrow of time and readout of the OTO correlator. We first discuss the realization of a simple nonlocal model with all-to-all spin couplings, where the overall sign is controlled by a quantum clock. Next we discuss a local lattice model, with nearest-neighbor couplings. The former is easier to implement while the latter is more relevant in a condensed-matter context. The advantage of a nonlocal model is that it does not suffer from errors due to imperfection in couplings (see Sec. VB) and, furthermore, from a physics standpoint, all maximally chaotic models known so far are nonlocal [3,10,11] and thus worth exploring.

A. Nonlocal model

The model consists of N qubits located in a coupler cavity bus with Jaynes-Cummings (JC) interactions [34] as shown in Fig. 2. In addition, an ancilla cavity (our quantum clock) is coupled to the cavity bus dispersively. The entire system Hamiltonian is $H_s = H_0 + V$, where

$$\begin{aligned} H_0 &= \omega_a a^\dagger a + \omega_b b^\dagger b + \sum_{j=1}^N \frac{1}{2} \epsilon \sigma_j^z - \eta a^\dagger a b^\dagger b, \\ V &= \sum_j g_j (\sigma_j^+ b + \text{H.c.}), \end{aligned} \quad (9)$$

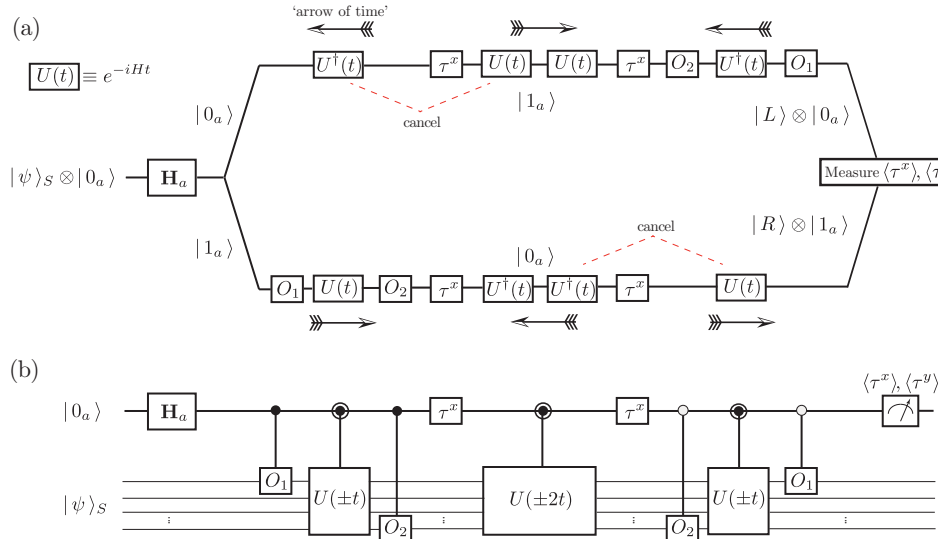


FIG. 1. (a) Illustration of the Ramsey interferometry protocol. The interferometry starts from the left, with the initial state $|\psi\rangle_S \otimes |0_a\rangle$. The Hadamard rotation splits the time evolution of the many-body state $|\psi\rangle_S$ into two branches, conditioned by the ancilla (quantum clock). The time evolution conditioned by clock state $|0_a\rangle$ ($|1_a\rangle$) is forward (backward) in the beginning. After applying the τ^x operations, the clock states on the two branches interchange and so are the directions of time evolution. The red dashed lines show the canceled time evolution. Conditional operations O_1 and O_2 on either branch are applied. A final measurement of the clock in the x and y basis gives the real and imaginary parts of the OTO correlator. We emphasize that the actual experimental time always goes from left to right. (b) Quantum circuit description of the same protocol.

where a^\dagger (b^\dagger) is the creation operator associated with the clock (bus) and ω_a (ω_b) is the corresponding frequency; σ_j^z is the j th qubit operator and ϵ is the corresponding frequency. We require these three frequencies to be detuned away from each other so that there is no exchange between different types of excitations. In particular, we choose $\epsilon < \omega_b$. We define the detuning between qubits σ_j and the bus b as $\Delta_b = \epsilon - \omega_b$. The last term in H_0 is the cross-Kerr interaction (with strength η) between the bus b and clock a cavities, which can be experimentally

realized, e.g., by coupling two superconducting cavities with a Josephson junction [58]. An alternative realization of the clock a could be a superconducting transmon qubit [59].⁴ In order to make sure that the clock and the bus are off-resonance and hence dispersively coupled, we require $\eta \ll |\omega_b - \omega_a|$. Finally, in the JC interaction term V , g_j is the interaction strength between the bus and system qubits, which in general can depend on the qubits' locations and can also be disordered.

The clock photon number n_a is a good quantum number since $[a^\dagger a, H_S] = 0$. For our use of a binary clock, we restrict H_S in the $n_a = 0$ and $n_a = 1$ sectors. This can be ensured when nonlinearity is introduced (see Appendix A for details). We can hence divide the system Hamiltonian into the two clock sectors, i.e., $H_S = \sum_{n_a=0,1} H_{S,n_a} |n_a\rangle\langle n_a|$. The form of V does not depend on the clock photon number, while H_0 can be rewritten as

$$H_0 = \sum_{n_a=0,1} \left[\omega_a n_a + (\omega_b - \eta n_a) b^\dagger b + \frac{1}{2} \epsilon \sum_j \sigma_{j,j+1}^z \right] \times |n_a\rangle\langle n_a|. \quad (10)$$

From this equation we can see clearly that the bus frequency is controlled by the clock state. For convenience, we introduce the clock-state-dependent detuning $\Delta_{b,n_a} = \Delta_b + \eta n_a$.

We now treat V perturbatively in the dispersive regime ($g_j \ll |\Delta_{b,n_a}|$) for both clock sectors and integrate out the bus and finally project to the $n_b = 0$ sector. The resulting effective Hamiltonian [15,16,18,61] up to the second order in

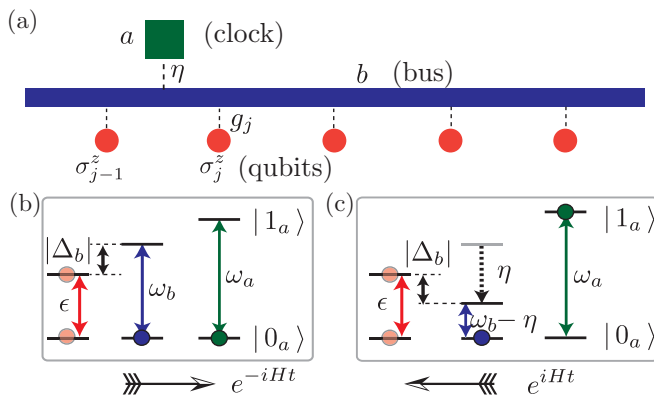


FIG. 2. Schematic diagrams of a cavity-QED implementation of an all-to-all coupled spin model. (a) Illustration of the many-body system, consisting of system qubits (red circles), a coupling cavity (blue bar) serving as a passive quantum bus, and an ancilla cavity (green square) serving as a quantum clock. (b) When there is no photon in the clock, the bus frequency ω_b is above the qubit frequency ϵ , with a negative detuning $\Delta_b < 0$. (c) When there is one photon in the clock, the bus frequency $\omega_b - \eta$ is pushed down below the qubit frequency ϵ by a distance $|\Delta_b|$, which inverts the sign of the detuning and hence the sign of the controlled Hamiltonian.

⁴The transmon qubit is often treated as a weakly anharmonic oscillator [60].

perturbation theory⁵ is

$$H_{\text{eff}} = H_0 + \left[\sum_{j,j'} \frac{g_j g_{j'}}{\Delta_{b,n_a}} \sigma_j^+ \sigma_{j'}^- + \sum_j \frac{1}{2} \frac{g_j^2}{\Delta_{b,n_a}} \sigma_j^z \right] |n_a\rangle \langle n_a| + \mathcal{O}\left(\frac{g_j^4}{\Delta_{b,n_a}^3}\right). \quad (11)$$

The first term at the second order is the so-called quantum-bus interaction, i.e., the flip-flop interaction mediated by the virtual photon in the cavity bus [18,61]. The second term represents the Lamb shift induced by the bus. These couplings of both terms depend on the detuning Δ_{b,n_a} , which is controlled by the clock state $|n_a\rangle$. In order to reverse the sign of these prefactors, we choose the cross-Kerr nonlinearity η such that $\Delta_{b,1} = -\Delta_{b,0} = -\Delta_b$, which leads to the condition

$$\eta = -2\Delta_b = 2(\omega_b - \epsilon). \quad (12)$$

The whole scheme is illustrated in Figs. 2(b) and 2(c). When enforcing this condition, the effective Hamiltonian in the rotating frame can be written as

$$\tilde{H}_{\text{eff}} = (1 - 2a^\dagger a) \left[\sum_{j < j'} \frac{g_j g_{j'}}{\Delta_b} (\sigma_j^+ \sigma_{j'}^- + \text{H.c.}) + \sum_j \frac{1}{2} \frac{g_j^2}{\Delta_b} \sigma_j^z \right] + \mathcal{O}\left(\frac{g_j^4}{\Delta_b^3}\right). \quad (13)$$

Here the effective Hamiltonian has exactly the form suggested in Eq. (2) and the arrow of time is controlled by the clock photon number $n_a = 0$ or 1 as desired. As shown above, the Hamiltonian controlled by the clock is an all-to-all coupled XY model in the presence of external field.⁶ Finally, we note that the presence of the Lamb shift is crucial for implementing the controlled operations mentioned in Sec. II, as will be explained in detail in Sec. IV.

B. Local model

Now we discuss the realization of local lattice models, in particular, we want the target Hamiltonian H to be a nearest-neighbor spin-1/2 XY -spin model. The scheme is illustrated in Fig. 3. The blue squares represent local cavities associated with photon operators b_j , which play the role of active degrees of freedom. The coupling of each neighboring

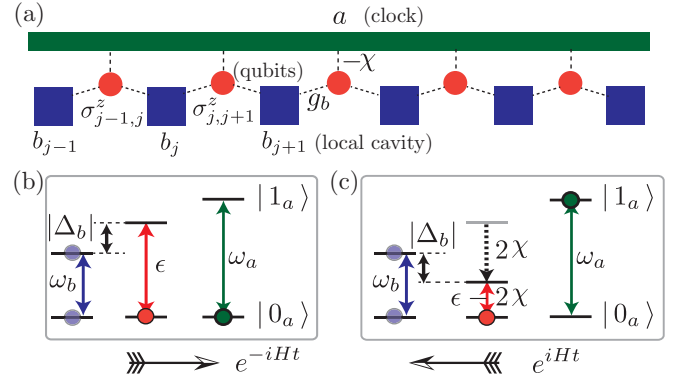


FIG. 3. Schematic diagrams of the cavity-QED implementation of a local model. (a) Illustration of the many-body system, consisting of local cavities (blue squares), qubits (red circles) mediating interactions between the cavities, and a global control cavity (green bar) serving as a quantum clock. (b) When no photon is present in the clock, the qubit energy ϵ is above the local cavity frequency ω_b , with a positive detuning Δ_b . (c) When a single photon is present in the clock, the qubit level spacing $\epsilon' \equiv \epsilon - 2\chi$ is pushed down below the local cavity frequency ω_b by a distance Δ_b , which inverts the sign of the detuning and hence the sign of the controlled Hamiltonian. We note that, in (b) and (c), the level diagram represents the level spacings rather than absolute energy levels.

cavity is mediated by qubits (red circles, associated with Pauli operators $\sigma_{j,j+1}^z$), which are also coupled to the global clock cavity a . These qubits are passive degrees of freedom and will be eventually integrated out. This scheme is different from the nonlocal Hamiltonian of the previous section, where the σ were active degrees of freedom while the b were passive. We considered this configuration so that the global degree of freedom remains a cavity photon. Similar to the previous section, the Hamiltonian is given by $H_s = H_0 + V$:

$$H_0 = \omega_a a^\dagger a + \omega_b \sum_j b_j^\dagger b_j + \frac{1}{2} \epsilon \sum_j \sigma_{j,j+1}^z - \chi a^\dagger a \sum_j \sigma_{j,j+1}^z, \quad (14)$$

$$V = g_b \sum_j [b_j^\dagger (\sigma_{j,j+1}^- + \sigma_{j-1,j}^-) + \text{H.c.}].$$

In place of the cross-Kerr interaction in Eq. (9), the last term in H_0 now represents the dispersive interaction between the global cavity a and the qubits σ with interaction strength χ . For convenience, we define ϵ as the renormalized frequency of the qubits, with the Lamb shift due to the global cavity already absorbed into the definition.

We note that the dispersive interaction can arise from junction couplers as described in the previous section or alternatively from a Jaynes-Cummings interaction in the dispersive regime [14,18], where we get $\chi = g_a^2 / \Delta_a$. Here g_a is the JC interaction strength and $\Delta_a = \omega_a - \epsilon$ is the detuning between the bare qubit σ and global cavity a frequencies. For weakly anharmonic superconducting qubits such as transmons, the derivation of the dispersive interaction can be found in Ref. [60].

⁵The third-order term is zero in this model. The complete formula of the second-order effective Hamiltonian without projecting onto the zero-qubit excitation subspace is shown in Appendix C.

⁶The fourth-order perturbative terms correspond to a ZZ interaction [35] in the form of $V_{ZZ} = (1 - 2a^\dagger a) \sum_{j < j'} \frac{2g_j^2 g_{j'}^2}{\Delta_b^3} \sigma_j^z \sigma_{j'}^z$. The ZZ interaction strength can be made stronger than this if one uses the transmon qubits [59], where the third level of the transmon contributes significantly to the ZZ interaction [35]. Additionally, there exist two other types of effective interactions, namely, the four-spin ring exchange interaction $\sigma_i^+ \sigma_j^- \sigma_k^+ \sigma_l^-$ and three-spin assisted hopping $\sigma_i^z \sigma_j^+ \sigma_k^-$.

Similar to the nonlocal case, the photon number n_a is a conserved quantity and we can restrict the system to zero- and one-photon sectors. In the following, we want to eliminate the qubit degrees of freedom σ perturbatively and find an effective Hamiltonian for which local cavities b form an XY model of which the sign is determined by the clock photon number.

We consider the dispersive regime where the local cavities and qubits are far detuned in both clock sectors compared to the JC interaction strength, namely,

$$\Delta_{b,n_a} = \epsilon - 2n_a\chi - \omega_b \gg g_b \quad (n_a = 0, 1).$$

Here $\Delta_{b,0} \equiv \Delta_b = \epsilon - \omega_b$ is the bare detuning in the absence of a clock photon, while $\Delta_{b,1} = \Delta_b - 2\chi$ represents the modified detuning in the presence of a clock photon due to the dispersive shift. In this regime, since the JC interaction is detuned, there is effectively no exchange of excitations between the local resonators and qubits. This leads to separate conservation of the total photon number in the local resonators $N_b = \sum_j b_j^\dagger b_j$ and total qubit excitations $S_z = \sum_j \sigma_j^z$. In particular, we are interested in the low-energy sector in which all the qubits have zero excitations, i.e., $|\downarrow\downarrow\downarrow\cdots\rangle$, which corresponds to a projector $P_{S_z=0}$.⁷ We can adiabatically eliminate the qubits by a Schrieffer-Wolff transformation [62,63] in each clock sector, namely, $H_{\text{eff},n_a} = P_{S_z=0} e^{S_{n_a}} H e^{-S_{n_a}} P_{S_z=0}$. Such a transformation can be done perturbatively by decomposing the effective Hamiltonian and generator S according to different orders in interactions strength g_b , i.e., $H_{\text{eff},n_a} = \sum_m H_{n_a}^{(m)}$ and $S_{n_a} = \sum_m S_{n_a}^{(m)}$. The first-order generator is given by

$$S_{n_a}^{(1)} = \frac{g_b}{\Delta_{b,n_a}} \sum_j b_j (\sigma_{j-1,j}^+ + \sigma_{j,j+1}^+) - \text{H.c.}, \quad (15)$$

which leads to the effective Hamiltonian (up to second order)

$$H_{\text{eff}} = \left(\omega_a n_a + \omega_b \sum_j b_j^\dagger b_j - \sum_{n_a} \frac{g_b^2}{\Delta_{b,n_a}} \sum_j [(b_j^\dagger b_{j+1} + \text{H.c.}) + 2b_j^\dagger b_j] \right) |n_a\rangle \langle n_a| + \mathcal{O}\left(\frac{g_b^4}{\Delta_{b,n_a}^3}\right). \quad (16)$$

We want detunings Δ_{b,n_a} ($n_a = 0, 1$) to have the same magnitude and opposite signs for different occupation number n_a . In other words, we need $\Delta_{b,1} = -\Delta_{b,0} = -\Delta_b$. To achieve this, we simply choose

$$\chi = \Delta_b = \epsilon - \omega_b. \quad (17)$$

In the situation that the dispersive interaction is realized by the Jaynes-Cummings interaction, i.e., $\chi = g_a^2/\Delta_a$, the above requirement becomes

$$g_a = \sqrt{\Delta_a \Delta_b}, \quad (18)$$

⁷We note that in this situation, if the dispersive interaction H_{disp} is realized by the JC interaction perturbatively, the nonlocal second-order flip-flop interactions between the qubits [Eq. (11)] do not play any role, since all the qubits are in the down states. Therefore, the dispersive Hamiltonian H_{disp} is indeed a valid description.

meaning that the JC interaction strength should be the geometric mean of two detunings with opposite signs. The whole scheme is illustrated in Figs. 3(b) and 3(c), where we have chosen the parameter such that $\omega_b < \epsilon < \omega_a$ and χ is hence positive.

When enforcing the condition in Eq. (17), the effective Hamiltonian in the rotating frame can be written as

$$\tilde{H}_{\text{eff}} = -\frac{g_b^2}{\Delta_b} (1 - 2a^\dagger a) \sum_j [(b_j^\dagger b_{j+1} + \text{H.c.}) + 2b_j^\dagger b_j] + \mathcal{O}\left(\frac{g_b^4}{\Delta_b^3}\right). \quad (19)$$

Here the effective Hamiltonian has exactly the form suggested in Eq. (2) and the arrow of time is controlled by the clock photon number $n_a = 0$ or 1 as desired. In addition, one can introduce strong optical nonlinearity to the local cavities, by embedding qubits into it. In this case, the photons in the cavities can be thought of as hard-core bosons due to photon blockade [13,21], i.e., $b_j^2 = b_j^{\dagger 2} = 0$, as long as the nonlinearity is much larger than the effective hopping strength between the resonators g_b^2/Δ_b . Hence \tilde{H}_{eff} actually describes an XY -spin model since the hard-core photon is equivalent to a spin-1/2 degree of freedom. Besides the flip-flop (XY) interaction, there is also a frequency shift with strength $2g_b^2/\Delta_b$ of the photon, of which the sign flips when the arrow of time is reversed. This frequency shift plays a similar role of effective magnetic field applied to the spins in the z direction, due to the mapping $Z_j = 2b_j^\dagger b_j - 1$. The shift is crucial because we need a conditional operation as mentioned in Sec. II, which only acts on the system evolving either forward or backward in time. This will be explained in detail in Sec. IV. The detailed architecture of a circuit-QED network and superconducting qubit array in a 3D cavity is explained in Appendix A and the numerical diagonalization of the original [Eq. (14)] and effective [Eqs. (16) and (19)] Hamiltonians is compared in Appendix B.

IV. QUANTUM OPTICAL REALIZATION

We briefly present the potential realization of models presented in the previous section and argue that such models could be implemented with current technology. While such models can be realized in most of quantum simulation platforms, ranging from cavity QED [13–16] to Rydberg atoms [29–32], and trapped ions [33] systems, motivated by recent advances in superconducting circuits, we focus our discussion on circuit-QED architecture.

Specifically, we consider a 2D on-chip circuit-QED quantum simulator consisting of a hybrid resonator-qubit network, pioneered by a series of proposals and experiments [19–25,28,54]. For the nonlocal model schematically shown in Fig. 2, each component could be implemented as follows: the superconducting qubits (red), the transmission-line resonator (blue) as the coupling bus, and the clock implemented by a transmission-line resonator or transmon qubit (green). For the local model shown in Fig. 2(a), the implementation is the superconducting qubits (red), the local superconducting transmission-line resonators (blue), and the global transmission-line resonator (green) as the clock. The

details about this architecture and an alternative realization with a qubit array in a 3D superconducting cavity can be found in Appendix A.

The parameter regime required to implement our models (Sec. III) is within the reach of current technology. The typical qubit and resonator frequencies can span the range from 100 MHz to 15 GHz and the typical JC interaction strength ranges from 0 to 400 MHz [23]. For the nonlocal model, the coupling strength η of the cross-Kerr term is a fraction (1/24) of the Josephson energy of the coupling junction E_J (ranging from 200 MHz to 20 GHz) [64,65] and so η can range from 10 MHz to 1 GHz. Further *in situ* tunability can be accessed by varying the flux through a junction-inductor loop, i.e., the so-called gmon coupler [65]. Therefore, the following hierarchy of parameters for the nonlocal model (Sec. III A) can be satisfied: $g_j \ll |\Delta_b| \sim \eta \ll |\omega_b - \omega_a|$. Thus, both the condition for sign flipping [Eq. (12)] and the requirement of dispersive coupling can be satisfied.

On the other hand, the following hierarchy of parameters for the local model (Sec. III B) can be realized: $g_b \ll |\Delta_b| \sim \chi$ or equivalently $g_b \ll |\Delta_b| < g_a \ll |\Delta_a|$. In this case, both the condition for sign flipping [Eq. (17) or (18)] and the requirement of the dispersive regime can also be satisfied. Moreover, within this parameter regime, our approximations to obtain the effective Hamiltonian [Eq. (16)] are valid, as we discuss in Appendix C. Specifically, the energy spectra of the full and the effective Hamiltonians are within 0.1% of each other (for $g_b/\Delta_b = 0.1$).

With the state-of-the-art technology, the 2D resonator-qubit network can contain ~ 100 qubits or resonators [28], while the 3D cavity with a typical dimension (e.g., 2.5 cm wide, 3 cm deep, and 1 cm high) can contain ~ 30 qubits [27]. The typical coherence time of a superconducting qubit is $t_{\text{coh}} = 1/\kappa \sim 100 \mu\text{s}$ (where $\kappa \sim 10$ kHz) [23]. The local resonators and clock cavity can typically have a longer coherence time $t_{\text{coh}} = 1/\kappa \sim 200 \mu\text{s}$ (where $\kappa \sim 5$ kHz) [23]. The characteristic interaction strength of the many-body system is determined by the dispersive interaction, the maximum of which can reach the strength $g^2/\Delta_b \sim 100$ MHz (for example, with $g = 400$ MHz and $\Delta_b = 1.5$ GHz) [23], corresponding to a local thermalization time $t_{\text{th}} \sim 10$ ns. The scrambling time is typically even smaller than the local thermalization time and hence is much smaller than the coherence time of the qubits or resonators and clock cavity. Therefore, the observation of scrambling behavior within the coherence time is unlikely.

One other key ingredient in implementing our protocol in Sec. II is the conditional operation

$$C_{O_1,0} = O_1 \otimes |0_a\rangle\langle 0_a| + \mathbb{I}_S \otimes |1_a\rangle\langle 1_a|$$

that only acts on the branch with the clock state $|0_a\rangle$. This can be realized with the dispersive shifts. For the local model discussed in Sec. III B, the simplest case is to choose $O_1 = X_{j_i} \equiv b_{j_i}^\dagger + b_{j_i}$ (in the zero- and one-photon subspace), meaning that $C_{O_1,0}$ becomes a CNOT gate. The dispersive shift of the local resonators $(2a^\dagger a - 1)2g_b^2/\Delta_b$ in Eq. (19) depends on the global control photon (qubit) state, which gives the opportunity to realize a CNOT gate by applying a π pulse on the local resonator with frequency $\omega_b - 2g_b^2/\Delta_b$. The hard-core photon state of the local resonator is only flipped in the branch

with clock state $|0_a\rangle$ due to the resonance condition. Similarly, a conditional operation $C_{O_1,1}$ that only accesses the branch with clock state $|1_a\rangle$ can be applied when sending a π pulse with frequency ω_b . One could achieve an arbitrary conditional single-qubit rotation by sending pulses with one of the two corresponding frequencies. A similar procedure can be applied to the nonlocal model discussed in Sec. III A, where the Lamb shift in Eq. (13) contributed to the conditional operations.

V. QUANTUM CLOCK VERSUS CLASSICAL SWITCH: IMPERFECTION AND ERROR ANALYSIS

In this section we analyze the stability of protocol against imperfection in the quantum clock and compare it with a previously proposed measurement scheme based on using a classical switch to control the arrow of time [12] during the protocol. The main advantage of our protocol is that we do not change the Hamiltonian during the protocol and therefore no statistical error corresponding to the fluctuation of the Hamiltonian will be incurred.

A. Classical switch

Recently, a protocol was proposed for measuring the same correlator [12] where a continuous classical switch is used to flip the sign of the Hamiltonian, i.e., from H to $-H$. In this type of protocol, one flips the overall sign of the Hamiltonian by changing the detuning in the cavity-QED system.

In order to make the comparison more concrete, we review the protocol with a classical switch from Ref. [12] in Fig. 4. In this protocol, an ancilla qubit is initially prepared in an equal superposition $\frac{1}{\sqrt{2}}(|0_a\rangle + |1_a\rangle)$ by the Hadamard gate. The ancilla is used to perform the conditional operation O_1 rather than controlling the sign of the Hamiltonian or equivalently the arrow of time. Therefore, the arrows of time in both branches always agree with each other. In the middle of the protocol, the sign of the Hamiltonian is flipped ($H \rightarrow -H$) with a continuous classical switch. However, since the detuning is a continuous variable, the change of the sign cannot be perfect

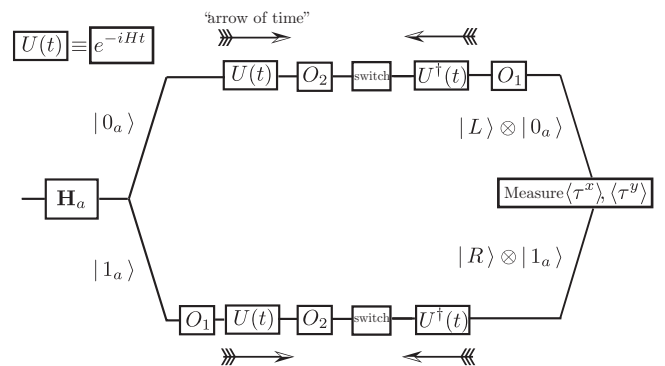


FIG. 4. Measurement protocol using a classical switch to control the arrow of time. An ancilla qubit is initialized as the superposition of $|0_a\rangle$ and $|1_a\rangle$ and hence splits the evolution into two branches in order to show the Ramsey interference. The ancilla enables conditional- O_1 operation but does not control the sign of the Hamiltonian. Another classical switch (such as the detuning) is used to change the sign of the Hamiltonian and hence flip the arrow of time.

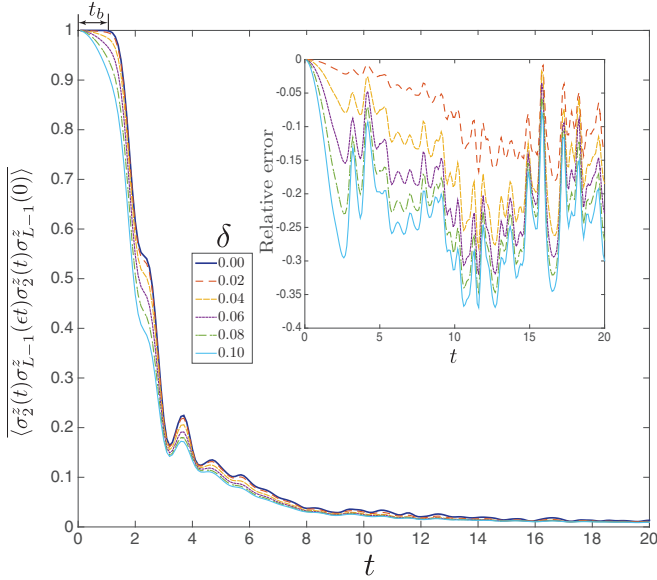


FIG. 5. Effect of imperfect sign change via classical switch for a spin model. The model considered here is $H = \sum_i (\tilde{\sigma}_i \cdot \tilde{\sigma}_{i+1} + h_i \sigma_i^z)$, where the h_i are chosen randomly from a uniform distribution in the interval $[-0.5, 0.5]$. The correlator $\langle O_2(t) O_1(t \epsilon) O_2(t) O_1(0) \rangle$ is shown, with $O_1 = \sigma_2^z$ and $O_2 = \sigma_{L-1}^z$, where $L = 12$ is the total number of sites. We take ϵ to be a random Gaussian variable with variance δ and averaging in $\langle O_2(t) O_1(t \epsilon) O_2(t) O_1(0) \rangle$ is performed over this ensemble. The inset shows the relative error $\langle O_2(t) O_1(t \epsilon) O_2(t) O_1(0) \rangle / \langle O_2(t) O_1(0) O_2(t) O_1(0) \rangle - 1$.

and the corresponding error can vary from one measurement shot to the next. We model this error by $-(1 + \epsilon)H$ as the flipped Hamiltonian, where ϵ is a random variable. Under this assumption, the final many-body wave functions in the two branches become

$$\begin{aligned} |R\rangle &= e^{iHt(1+\epsilon)} O_2 e^{-iHt} O_1 |\psi\rangle_S, \\ |L\rangle &= O_1 e^{iHt(1+\epsilon)} O_2 e^{-iHt} |\psi\rangle_S, \end{aligned} \quad (20)$$

which leads to the overlap

$$\begin{aligned} &{}_S \langle \psi | e^{iHt} O_2 e^{-iHt(1+\epsilon)} O_1 e^{iHt(1+\epsilon)} O_2 e^{-iHt} O_1 | \psi \rangle_S \\ &= \langle O_2(t) O_1(\epsilon t) O_2(t) O_1(0) \rangle. \end{aligned}$$

In contrast to the error incurred in the quantum clock, which is independent of the time t (see the next section), here the error is a function of $t\epsilon$ and the correlation function only matches the desired OTO correlator in the limit $\epsilon t \ll 1$. In other words, since the value of ϵ is not *a priori* known, one measures the average of the above correlators. Figure 5 shows the time dependence of the OTO correlator of a Heisenberg model with a random external field. Multiple curves in the presence of the random error ϵ with mean zero and different variance δ are shown. The error made is clearly time dependent, which potentially makes extracting the functional dependence of the correlator at short times (e.g., to understand scrambling) challenging.

In particular, for the early-time behavior, the curve without error ($\delta = 0$) shows an onset time $t_b \approx 1$, after which the OTO correlator begins to rapidly decrease, i.e., the scrambling behavior starts. The onset of scrambling could be understood by introducing the butterfly velocity v_b [46,47]. Specifically,

the early-time behavior of OTO correlators, in the fast scrambling regime, can be approximated by

$$C_{\text{OTO}} \approx 1 - e^{\lambda(t-x/v_b)}, \quad (21)$$

where x is the distance between O_1 and O_2 and λ is the Lyapunov exponent. We note that this form is not universal and in some cases the exponential behavior is replaced by a power-law form, e.g., in many-body localized systems [48–52]. In Eq. (21) we see that the actual scrambling starts at $t_b = x/v_b$. This can be understood in the context of the Lieb-Robinson bound [66], where the propagation of operators is bounded by a light cone, characterized by the same velocity v_b . In particular, in the beginning ($t = 0$), the operators O_1 and O_2 commute with each other $C_{\text{OTO}} \approx \langle O_1(0) O_2(t) O_2(t) O_1(0) \rangle = 1$ (which means that $|L\rangle \approx |R\rangle$). As time evolves, the operator $O_2(t)$ grows linearly in time and forms a superposition of string operators. Eventually, at $t_b = x/v_b$, the string operators reach $O_1(0)$ and the OTO is no longer equal to unity. However, as we observe in Fig. 5, in the presence of error ϵ , the onset time t_b and the butterfly velocity v_b are significantly modified. For $\epsilon = 0.1$, t_b and v_b decrease approximately to zero. This is not surprising since the correlator $C_{\text{OTO}} \approx \langle O_1(\epsilon t) O_2(t) O_2(t) O_1(0) \rangle < 1$ decreases rapidly when ϵt increases. We see that this error not only affects the extraction of butterfly velocity, but also distorts the shape of the early-time behavior, which will make extracting functional dependence of the correlator (such as exponential or power-law growth) challenging.

B. Quantum clock

In the following we analyze three types of errors that could affect the efficiency of our protocol.

1. Imperfection in pulses

Both the initial Hadamard gate ($\pi/2$ pulse) and the τ^x operation (π pulse) that flips the clock and hence the arrow of time can suffer from errors since the rotation angles are continuous variables and hence may not be exact. For a rotation along certain axis \hat{n} , we can simply parametrize the rotation error as

$$R_{\hat{n}}(\theta + \delta\theta) = e^{-i(\theta + \delta\theta)\hat{n} \cdot \vec{\tau}/2},$$

where $\delta\theta$ is a small random fluctuation that differs in different shots of measurement.

Assuming that the initial Hadamard gate is perfect, we first consider the imperfection of the two τ^x flip operations on the clock ($\theta_1, \theta_2 = \pi$ and $\hat{n} = \hat{x}$). Note that because the two flips of the quantum clock divide both the upper and lower branches into three sectors, $2^3 = 8$ paths are generated. The two paths $|L\rangle$ and $|R\rangle$ always stay in either of the two branches, i.e., upper to upper to upper and lower to lower to lower, respectively, which are the only paths that survive in the absence of error, i.e., $\delta\theta_1, \delta\theta_2 = 0$. Once the error is present, the other six paths, which bounce between the upper and lower branches, will have nonzero amplitude. For example, the upper to lower to upper path corresponds to the weighted state $(-i \sin \frac{\delta\theta_1}{2})(-i \sin \frac{\delta\theta_2}{2})[U^\dagger(t)]^3 O_2 U^\dagger(t) O_1 |\psi\rangle_S$, while the upper to lower to lower path corresponds to the state $(-i \sin \frac{\delta\theta_1}{2})(\cos \frac{\delta\theta_2}{2})[U^\dagger(t)]^3 U(t) |\psi\rangle_S$. The errors modify the

final state in Eq. (7) to

$$|\Psi_f\rangle = \frac{1}{\sqrt{2}} \left[\left(\cos \frac{\delta\theta_1}{2} \cos \frac{\delta\theta_2}{2} |R\rangle + \sum_{i=1}^3 c_i |E_i\rangle \right) \otimes |1_a\rangle + \left(\cos \frac{\delta\theta_1}{2} \cos \frac{\delta\theta_2}{2} |L\rangle + \sum_{i=4}^6 c_i |E_i\rangle \right) \otimes |0_a\rangle \right]. \quad (22)$$

Here the states $|E_{1,2,3}\rangle$ ($|E_{4,5,6}\rangle$) coming from the other unwanted paths end up in the upper (lower) branch. Their amplitudes are $c_1 = c_4 = -i \sin \frac{\delta\theta_1}{2} \cos \frac{\delta\theta_2}{2}$, $c_2 = c_5 = -i \sin \frac{\delta\theta_2}{2} \cos \frac{\delta\theta_1}{2}$, and $c_3 = c_6 = \sin \frac{\delta\theta_1}{2} \sin \frac{\delta\theta_2}{2}$.

Note that the errors in the π pulse do not change the value of the Hamiltonians H and $-H$ for forward and backward propagation. Nor do the errors change the quantum states $|R\rangle$ and $|L\rangle$, of which the overlap $\langle L|R\rangle$ is the OTO correlator. Now the question is to what extent our protocol can extract this overlap from the unwanted noise \mathcal{N} . When we measure the τ^x operator according to the protocol, which leads to

$$\begin{aligned} \langle \tau^x \rangle_f &\equiv \langle \Psi_f | \mathbb{I} \otimes \tau^x | \Psi_f \rangle \\ &= \cos^2 \left(\frac{\delta\theta_1}{2} \right) \cos^2 \left(\frac{\delta\theta_2}{2} \right) \text{Re}[\langle L|R\rangle] + \mathcal{N}. \end{aligned} \quad (23)$$

The first term is a slightly shrunken signal proportional to the real part of the overlap between $|L\rangle$ and $|R\rangle$. The second noise term compares the real or imaginary part of the overlap involving the unwanted paths $|E_i\rangle$. Since the magnitude of the real or imaginary part of any overlap is bounded by 1, i.e., $|\text{Re}(\text{Im})\langle E_i|E_j\rangle| \leq 1$ and $|\text{Re}(\text{Im})\langle E_i|R(L)\rangle| \leq 1$, one can derive a bound for the noise, namely,

$$\begin{aligned} |\mathcal{N}| &\leq |\sin \delta\theta_1| + |\sin \delta\theta_2| + |\sin \delta\theta_1| |\sin \delta\theta_2| \\ &\quad + \sin^2 \left(\frac{\delta\theta_1}{2} \right) (1 + |\sin \delta\theta_2|) \\ &\quad + \sin^2 \left(\frac{\delta\theta_2}{2} \right) (1 + |\sin \delta\theta_1|) + \sin^2 \frac{\delta\theta_1}{2} \sin^2 \frac{\delta\theta_2}{2} \\ &= |\sin \delta\theta_1| + |\sin \delta\theta_2| + \mathcal{O}(\delta\theta_1^2 + \delta\theta_2^2 + \delta\theta_1 \delta\theta_2). \end{aligned} \quad (24)$$

This expression suggests that the noise bound is controlled by the errors on the rotation angles. The same prefactor and bound for noise hold for the τ^y measurement, corresponding to the imaginary part of the overlap. The signal-to-noise ratio \mathcal{S} of the overlap has the expression

$$\mathcal{S} \approx \frac{\cos^2 \left(\frac{\delta\theta_1}{2} \right) \cos^2 \left(\frac{\delta\theta_2}{2} \right)}{|\sin \delta\theta_1| + |\sin \delta\theta_2|} |\langle L|R\rangle|, \quad (25)$$

which is also controlled by the error angles and the magnitude of the overlap. Therefore, the overlap can be resolved once its magnitude is much larger than the noise background.

In addition, the imperfection in the initial Hadamard gate ($\theta' = \pi/2$, $\hat{n} = \hat{y}$) leads to the preparation of an unequal superposition of the two branches

$$|\psi\rangle_S \otimes \left(\sqrt{\frac{1 - \sin \delta\theta'}{2}} |0_a\rangle + \sqrt{\frac{1 + \sin \delta\theta'}{2}} |1_a\rangle \right).$$

The unequal weight of the wave functions in the two branches of the interferometer [conditioned by $|0_a\rangle$ and $|1_a\rangle$, respectively, as shown in Eq. (22)] remains in the final output $|\psi\rangle_f$. Therefore, the measurement outcome in the presence of both types of errors becomes

$$\begin{aligned} \langle \tau^{x(y)} \rangle_f &= \cos \delta\theta' \left\{ \cos^2 \left(\frac{\delta\theta_1}{2} \right) \cos^2 \left(\frac{\delta\theta_2}{2} \right) \right. \\ &\quad \left. \times \text{Re}(\text{Im})[\langle L|R\rangle] + \mathcal{N} \right\}. \end{aligned} \quad (26)$$

An extra prefactor $\cos \delta\theta'$ further shrinks the magnitude of the overlap. On the other hand, the phase of the overlap, i.e., $\arg[\langle L|R\rangle] = \arctan\{\text{Im}[\langle L|R\rangle]/\text{Re}[\langle L|R\rangle]\}$, is less affected by the three error angles since the same prefactors on both the real and imaginary parts cancel each other. The signal-to-noise ratio remains the same expression as in Eq. (25) since the same prefactor $\cos \delta\theta'$ is introduced to the noise term.

We emphasize that with the current quantum information technology such as circuit QED, the fidelity of a single-qubit gate can reach over 99.9% [67]. Therefore, errors in rotating angles are under control and will not change the order of magnitude of the signal and we have shown above that the signal is stable against a small imperfection in the gates.

2. Imperfection in the couplings

Before doing the experiments, one needs to tune the parameters such as the detunings Δ_a and Δ_b (e.g., by sweeping the magnetic fluxes penetrating the superconducting loops) to satisfy the conditions in Eq. (12), (17), or (18), which allows the reversing of sign exactly. In addition, there may be inhomogeneity in the qubit-cavity coupling, namely, the coupling strength may have a spatial dependence: $g \rightarrow g_j$ and $g_a \rightarrow g_{a,j}$. For the nonlocal model discussed in Sec. III A this is not a problem since the inhomogeneity only introduces disorder in the effective coupling strength but does not affect the condition (12), which allows exactly flipping the sign with the clock. However, for the local model discussed in Sec. III B, spatial-dependent tunability of the qubit frequency ϵ_j , or equivalently the tunability of detunings $\Delta_{a,j}$ and $\Delta_{b,j}$, is needed to satisfy the required conditions in Eq. (17) or (18). Once the tuning is done with high precision, the static imperfection is removed and no such errors will be introduced *in situ*.

The key is to have a calibration procedure that makes sure that the static imperfection is removed or under control. This can be achieved by a simplified version of the Ramsey interference protocol, without applying the operators O_1 and O_2 , such that the cancellation between the forward and the backward evolution could be verified.

3. Effects of the imperfections on the conditional operations

We note that the success of the protocol highly depends on the ability to perform conditional operations on a particular branch of the interferometer. The operation relies on the dispersive shifts of the nonlocal model [Eq. (13)] and local model [Eq. (19)], respectively.

Using the local model as an example, the dispersive shift term $(2a^\dagger a - 1)2g_b^2/\Delta_b \sum_j b_j^\dagger b_j$, which creates a frequency difference $4g_b^2/\Delta_b$ for the two branches conditioned by $|0_a\rangle$

and $|1_a\rangle$, is responsible for the conditional operation, since the applied pulses generating O_1 and O_2 need to be on resonance with the dressed resonator frequency $\omega_b - 4g_b^2/\Delta_b$ or ω_b in a particular branch. Now we consider the spatial disorder of the parameters, meaning that the dressed local-resonator frequency becomes $\omega_{b,j} - 4g_{b,j}^2/\Delta_{b,j}$ or $\omega_{b,j}$, respectively. As long as the frequency difference $4g_{b,j}^2/\Delta_{b,j}$ (typically on the order of 10–100 MHz for circuit-QED [23]) is much larger than spectral width of the pulses (typically on the order of 5–10 KHz [23]), the difference can be resolved by the pulses and the conditional operation can be applied. Once this condition is satisfied, the fidelity of the conditional operation is only limited by the typical fidelity of the single-qubit gate, which can reach 99.9% with the state-of-the-art circuit-QED technology [67].

We note that due to the spatial disorder of the parameters, the dressed local-resonator frequencies on the two sites hit by O_1 and O_2 are different. However, the spatial disorder is static, so the frequency difference is fixed among different shots of measurements. Therefore, one only needs to establish a benchmark by measuring the dressed frequencies of the two local-resonator sites hit by O_1 and O_2 , respectively, before starting the protocol. The benchmark can be done by sweeping the driving frequency and locating the resonance in the situation with and without a photon in the clock cavity.

VI. EXTENSIONS OF THE LOCAL MODEL

In Sec. III B we showed concretely how a 1D XY -spin model can be embedded with a global quantum clock to control the sign of the Hamiltonian. Here we extend the model in terms of the interaction, lattice type, spatial disorder, and dimensionality.

A. Soft-core photons and Hubbard model

Above we focused on hard-core photons that lead to effective spin-1/2 models. Now we consider soft-core photons, which allows one to build further interactions. Carrying out the Schrieffer-Wolff transformation to fourth order yields the following correction to the Hamiltonian in Eq. (16):

$$\begin{aligned} \Delta H_{\text{eff}} = & \sum_{n_a} \frac{g_b^4}{\Delta_{b,n_a}^3} \sum_j [2b_j^\dagger b_j^\dagger b_j b_j + 6b_j^\dagger b_j b_{j+1}^\dagger b_{j+1} + 8b_j^\dagger b_j \\ & + (2b_j^\dagger b_{j+1} + b_j^\dagger b_{j+2} + \text{H.c.}) + (b_{j+1}^\dagger b_j^2 + \text{H.c.})] \\ & \times |n_a\rangle \langle n_a| + \mathcal{O}\left(\frac{g_b^6}{\Delta_b^5}\right). \end{aligned} \quad (27)$$

From the above Hamiltonian, we see that all types of interactions, including the on-site interactions, nearest-neighbor density-density interactions, next-nearest-neighbor hoppings, and nearest-neighbor pair hoppings, depend on the detuning Δ_{b,n_a} . Therefore, we can easily change the sign of interactions by flipping detuning as we did before, namely, using the dispersive shift induced by the global cavity. When imposing the constraint (17) or (18) as before, the total effective Hamiltonian in the rotating frame [continuing the series in

Eq. (19)] is

$$\begin{aligned} \tilde{H}_{\text{eff}} = & (1 - 2a^\dagger a) \left[-\frac{g_b^2}{\Delta_b} \sum_j [(b_j^\dagger b_{j+1} + \text{H.c.}) + 2b_j^\dagger b_j] \right. \\ & + \frac{g_b^4}{\Delta_b^3} \sum_j [2b_j^\dagger b_j^\dagger b_j b_j + 6b_j^\dagger b_j b_{j+1}^\dagger b_{j+1} + 8b_j^\dagger b_j \\ & + (2b_j^\dagger b_{j+1} + b_j^\dagger b_{j+2} + \text{H.c.}) + (b_{j+1}^\dagger b_j^2 + \text{H.c.})] \\ & \left. + \mathcal{O}\left(\frac{g_b^6}{\Delta_b^5}\right) \right], \end{aligned} \quad (28)$$

which is actually an extended Bose-Hubbard model with extra pair-hopping terms and an embedded quantum clock controlling the sign of the Hamiltonian. We note that the faster scrambling behavior near the quantum critical point of a Bose-Hubbard model was recently discussed in Ref. [53].

B. Simulating disorder and localization

Above we constructed only the spatially uniform model. We now note that an XY or extended Hubbard model with spatial disorders in both the hopping strength and on-site and off-site interactions can also be designed. To do so, one simply makes the local JC interaction strength [Eqs. (19) and (28)] spatially disordered, i.e., $g_b \rightarrow g_{b,j}$. This disorder does not affect the detuning Δ_{b,n_a} that controls the sign of the Hamiltonian. Hence, the constraint (17) or (18) that determines the necessary condition to exactly reverse the sign does not change.

With the spatial disorder in the Hamiltonian, one can potentially realize models with Anderson localization or many-body localization [68]. The OTO correlator in these situations may be able to distinguish between a chaotic (ergodic) phase and a many-body localized phase [48–52].

C. Extension in dimensionality and realization

Generalization of our setup to 2D models is straightforward. One can devise a checkerboard lattice, with one sublattice formed by blue squares playing the role of active degrees of freedom and one sublattice formed by red circles that will be integrated out and only passively mediate the interactions between blue squares. Here one can go beyond the Jaynes-Cummings lattice (oscillator plus a two-level system) and assume that both the blue squares and red circles represent multilevel atoms (or artificial atoms such as transmons [59]), which can be viewed as qudits, or in simple cases anharmonic oscillators. The two types of atoms will be detuned from each other and have different level structures, while the interaction between them are of flip-flop (XY) type. The checkerboard lattice is placed in a global 3D cavity, where the cavity only interacts with the red atoms dispersively and shift their frequencies, as illustrated in Fig. 6. The method of such selective coupling is discussed in Appendix A. Considering the excitations of active (blue) atoms in the hard-core limit (equivalent to spin 1/2), an XY model similar to Eq. (19) in two dimensions can be derived with the Schrieffer-Wolff transformation. This can be easily seen in the limit when the red atom is strongly anharmonic and therefore can be treated

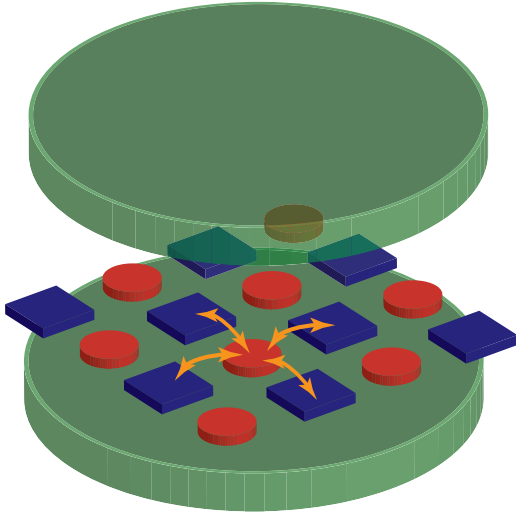


FIG. 6. A 2D generalization of the cavity-QED implementation. Two types of multilevel atoms (qudits), represented by blue squares and red circles, form a checkerboard lattice that is placed in a 3D cavity. The blue atoms play the role of active degrees of freedom, while the red atoms are passive coupler mediating interactions between red atoms. The two types of atoms are coupled by nearest-neighbor flip-flop interactions. The cavity is selectively coupled to only the red atoms with dispersive interaction to shift their frequencies.

as a two-level system (qubit), thus recovering the results of the JC lattice model.

Finally, we also note that such a checkerboard-lattice setup can also be implemented with Rydberg atoms, where an additional clock atom is dispersively coupled only to the sublattice serving as a passive coupler through the Rydberg blockade mechanism [30,36–38]. Such a partial addressing scheme has been discussed in a recent work about measuring the entanglement spectrum with Rydberg atoms [44].

VII. CONCLUSION AND OUTLOOK

In this work we showed that by embedding a quantum clock into a many-body system, one can control the direction of the time evolution of a many-body system. One can then use such a quantum clock to measure the out-of-time correlator, which characterizes chaos in a generic quantum many-body system. We have also constructed a class of models implementable in cavity- or circuit-QED systems in which such embedding is possible. With the state-of-the-art technology, one can have ~ 100 qubits or local resonators in a 2D on-chip resonator-qubit network and ~ 30 qubits in a 3D cavity. The typical performance time is limited by the coherence time of the qubits or resonators and clock cavities, which is on the order of $100 \mu\text{s}$ and hence much larger than the local thermalization time and scrambling time. In addition, we showed that our protocol, which utilizes a quantum clock, is robust against imperfection and statistical error in the single-qubit gate and hence is advantageous over a protocol using a classical switch, which is more sensitive to statistical errors. The fidelity of the protocol within coherence time is primarily limited by the

fidelity of the single-qubit gate, which can reach $\sim 99.9\%$ in the state-of-the-art circuit-QED technology.

Although we focused on realizations with cavity and circuit QED, the way we construct the models is generic and can be applied to many other platforms where coupling a clock qubit globally to the many-body system is possible, such as Rydberg atoms and ion traps. We also note that the ability to have quantum control of the time evolving direction of a many-body system can have many other applications, including the ability to measure a Loschmidt echo equivalent to ${}_S \langle \psi | e^{iHt} e^{-i(H+\delta H)t} | \psi \rangle_S$, which also requires evolving both backward and forward in time, and is an alternative measure of quantum chaos. It is also relevant for performing quantum phase estimation, a very useful tool to extract information from a generic quantum simulator without doing quantum-state tomography. From a condensed-matter perspective, probing the OTO correlator across the many-body localization-delocalization transition could be very pertinent since the key difference between a thermal phase and a many-body localized phase is precisely that the former is chaotic while the latter is not. As discussed in Sec. VI B, this is possible within our setup. Similarly, simulating SYK models [3,10] in cavity QED or cold atoms and measuring OTO correlators is another promising direction.

Conceptually, the idea of measuring OTO correlators using the quantum clock is reminiscent of the idea of quantum-controlled ordering of gates discussed in Ref. [69]. The basic result of Ref. [69] is that if in quantum computing one allows a control switch that switches the order in which gates are applied (a permutation switch), it reduces the computational complexity of certain problems from $O(n^2)$ to $O(n)$. It would be worthwhile to explore the possibility of obtaining such speedups in quantum algorithms using our cavity-QED setup.

ACKNOWLEDGMENTS

G.Z. and M.H. were supported by ONR-YIP, ARO-MURI, AFOSR-MURI, NSF-PFC at the JQI, and the Sloan Foundation. T.G. acknowledges startup funds from UCSD and fellowship from the Gordon and Betty Moore Foundation 852 (Grant No. 4304).

APPENDIX A: CIRCUIT AND CAVITY QED ARCHITECTURE REALIZING THE LOCAL MODELS

In this appendix we discuss details of the circuit-QED architecture, which realize our desired local model described by Eq. (14) and illustrated in Fig. 3, and the corresponding experimental protocols.

1. Two-dimensional circuit-QED network

We first discuss the realization with the 2D on-chip circuit-QED network and illustrate it in Fig. 7(a). As an example, we show in Fig. 7(a) the realization of qubits with the Cooper-pair box or transmon, composed of two Josephson junctions and one capacitor. The level structure and qubit frequency are tuned *in situ* by the external magnetic flux threading the junction loop. In general, any type of superconducting qubits can be used in the network, such as flux and fluxonium qubits [70–72].

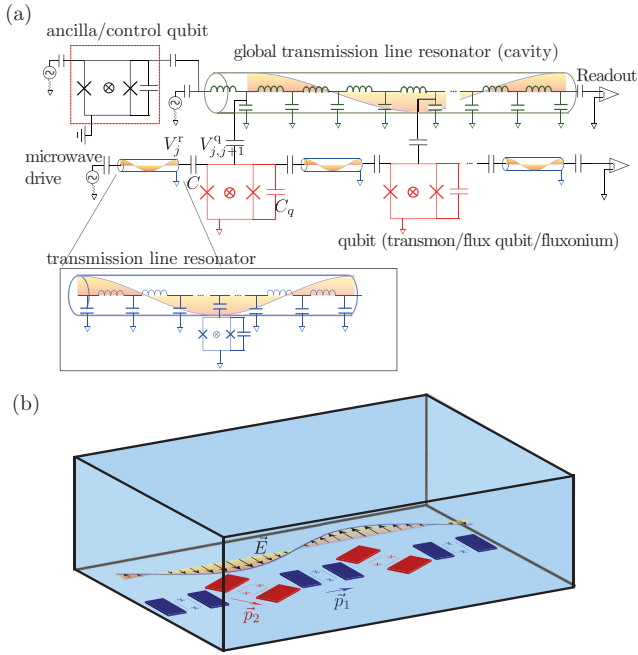


FIG. 7. Cavity- or circuit-QED architecture, which realizes the model described by Eq. (14) and illustrated in Fig. 3. (a) A 2D on-chip circuit-QED network. The setup consists of a global transmission-line resonator serving as the quantum clock; local transmission-line resonators, which play the role of active degrees of freedom; and qubits, which are passive degrees of freedom that mediate interactions between local resonators and are controlled by the global resonator. Alternatively, one can have an additional ancilla qubit coupled to the global resonator, which can either be used to manipulate the cavity photon state or be dispersively coupled to the local qubits mediated by the cavity bus and hence serves as the clock. (b) A 3D cavity QED with superconducting qubit array, with qubits of two different frequencies (represented as red and blue). The blue qubits play the role of active degrees of freedom, while the red qubits are passive couplers that mediate interactions between the blue qubits. The dipoles of the qubits are facing different directions to enable selective coupling to the global cavity.

The local λ -mode transmission-line resonators⁸ are coupled capacitively to the qubits [19]. We represent the voltage on the ends of the resonator as V_j^r and the electric charge on the upper superconducting island (nongrounded one) of the qubit as $V_{j,j+1}^q$. The capacitive coupling between resonator and qubit on its right leads to the interaction $T_j^{\text{right}} = CV_j^r V_{j,j+1}^q$, where C is the intermediate capacitance. Canonical quantization allows us to represent the phase variables with the creation or annihilation of photon operators, i.e., $V_j^r = V_{\text{rms}}^r (b_j + b_j^\dagger)$ and $V_{j,j+1}^q = eC_g \sigma_{j,j+1}^x$, where V_{rms}^r is the root-mean-square voltage of the resonator, C_q the qubit capacitance, and e the unit charge. Therefore, with a rotating-wave approximation that drops the counter-rotating term, the

⁸One could also choose the $\lambda/2$ mode, which is the fundamental mode of the resonator, leading to the opposite sign of the phase variable on the two ends. However, eventually the sign can be gauged in a 1D chain.

interaction can be expressed as the Jaynes-Cummings form $T_j^{\text{right}} = g_b (b_j^\dagger \sigma_{j,j+1}^- + \text{H.c.})$, where the JC interaction strength is $g_b = 2eC_q V_{\text{rms}}^r$. The interaction between the resonator and the qubit on its left has an identical expression. The sum of all the pairwise interaction terms leads to the realization of the JC interaction V in Eq. (14). Since we eventually need hard-core bosons to simulate spin models, we introduce nonlinearity into the resonators by embedding qubits, which is illustrated in the inset of Fig. 7(a). The presence of the qubit inside the resonator leads to photon blockade [21].

The global transmission-line resonator (cavity) is coupled to all the qubits between the local resonators. In order to make sure the coupling is uniform, we put the qubits in the peaks (positive or negative) of the resonator mode, implying that the length of the resonator is at least $N\lambda/2$, where λ is the microwave wavelength and N is the total number of qubits. This also means that the control photon occupies the N th-harmonic mode. Such a superlong transmission-line resonator has been explored experimentally in Ref. [73]. Due to the dressing of the qubit, the level structure of the global resonator also becomes anharmonic, therefore allowing one to manipulate the photon state in the truncated zero- and one-photon subspace.

In addition, one could add another ancilla qubit coupled to the global cavity. Instead of exploiting the nonlinearity of the global resonator, one could also use an ancilla qubit to manipulate the photon state through the combination of the controlled-phase gate induced by dispersive interaction and single-qubit rotation [14].

An alternative way to realize the dispersive-type coupling is to directly couple the ancilla qubit (represented by Pauli operator τ) to all the local qubits, mediated by the virtual photon in the cavity. In this case, the cavity serves as a quantum bus and hence has no photon occupation. One subtle point is that multiple modes are mediating the dispersive interaction, however, one can select one to play a major role by tuning the qubit frequency close to the frequency of the selected mode. When the global control qubit is detuned from local qubits, the only interaction surviving the rotating-wave approximation is the ZZ coupling

$$H_{\text{disp}} \rightarrow H_{ZZ} = -\frac{\chi'}{2} \tau^z \sum_j \sigma_{j,j+1}^z. \quad (\text{A1})$$

Such a ZZ interaction is frequently used for a controlled-phase gate on many platforms. For example, in circuit QED, such a ZZ interaction exists due to the contribution of the third level of the transmon qubits [35]. One can easily see that by making the replacement $\tau^z = 1 - 2a^\dagger a$ in the zero- and one-photon subspace, the above H_{ZZ} is formally identical to H_{disp} [in Eq. (14)] up to a constant frequency shift, which can be absorbed into the renormalized local qubit frequency ϵ .

An alternative for the global transmission resonator can be a resonator array [19,20,23,54], where we can use the common mode ($k=0$) as the clock. Besides the above approach using capacitive coupling and the JC interaction to generate the dispersive interaction perturbatively, one can also directly couple each resonator in the array to the qubits with a Josephson junction [58,60]. In this way, the dispersive interaction strength χ is only proportional to the Josephson energy E_J and does not depend on the detuning in the form of

g_a^2/Δ_a and hence can remain sizable even when the resonator and qubit are far detuned. With this method, the condition (17) for sign flip is even easier to satisfy.

2. Three-dimensional cavity-QED with superconducting qubit array

Now we consider a 3D version of the experimental realization. Instead of considering a hybrid resonator-qubit network as mentioned above, here we only consider a superconducting qubit array in a 3D cavity [cf. Fig. 7(b)]. The word ‘‘qubit’’ here is not restricted to two-level systems, but actually refers to multilevel artificial atoms, which is an accurate description for any superconducting qubits, such as transmons [59]. Experimental realization of a Bose-Hubbard model with a transmon array in a 3D cavity was achieved recently in Ref. [26]. Still, the array consists of two different types of artificial atoms [illustrated with red and blue in Fig. 7(a)] with different level structures, achieved, for example, by choosing a different size of the junction loop between the two superconducting islands. The red qubits play the role of passive couplers that mediate interactions between the blue qubits, consistent with the schematic diagram in Fig. 2(a).

In order to only couple the red qubits but not the blue qubits to the 3D cavity, we exploit the directional property of dipole coupling and so choose different orientations of the red and blue qubits. As illustrated in Fig. 7(b), the dipole of the blue qubits \vec{p}_1 , originating from the Cooper pair tunneling between the two islands, is perpendicular to the cavity electric field \vec{E} . Therefore, the dipole interaction for the blue qubits $\vec{p}_1 \cdot \vec{E}$ is zero. On the other hand, the dipole of the red qubits \vec{p}_2 is rotated so as not to be perpendicular to the electric field, which in the end gives rise to the dispersive interaction H_{disp} in Eq. (14). An alternative trick of realizing selective coupling, also illustrated in Fig. 7(b), is by placing the red (blue) qubits in the peaks (nodes) of the cavity mode.

By treating the two types of qubits (artificial atoms) as anharmonic oscillators, an effective Hamiltonian similar to Eq. (19) can be derived with the Schrieffer-Wolff transformation up to second order. The scheme can be easily generalized to two dimensions, such as the checkerboard lattice shown in Fig. 6.

APPENDIX B: NUMERICAL VERIFICATION OF THE EFFECTIVE HAMILTONIAN

In order to verify the effective model we constructed from perturbation theory, we need to compare it with the exact numerical diagonalization of the original Hamiltonian. In particular, we choose to verify the local model we constructed in Sec. III B, which has higher complexity than the all-to-all coupled spin model discussed in Sec. III A. In this appendix we compare the numerical diagonalization of the original model (14) and the full second-order effective Hamiltonian (16) or (19).

We start with the simplest dimer case as shown in Fig. 8(a), containing two local cavity sites, and a qubit in between that is coupled to the clock cavity. We choose the following specific parameters (which can potentially be realized with circuit-QED systems): $\Delta_b = 50$ MHz, $\Delta_a = 800$ MHz, $\chi = 50$ MHz

(or equivalently $g_a = 200$ MHz if the dispersive interaction arises from the global Jaynes-Cummings interaction perturbatively), and on-site photon cutoff $n_b^{\text{max}} = 3$; we vary g_b in the simulation. In particular, we choose the parameters such that the conditions (17) and (18) are always satisfied so the sign of the effective Hamiltonian can be flipped by the clock. In Fig. 8(b) we compare the spectrum E_v of the original (blue circles) and second-order effective Hamiltonian (yellow squares) at $g_b/\Delta_b = 0.1$ ($\Delta_b = 50$ MHz and $g_b = 5$ MHz), which is deep in the dispersive regime, and the perturbation is expected to be valid. The spectrum can be obviously divided into two sectors corresponding to $n_a = 0$ and $n_a = 1$ and the exact and perturbation results match very well throughout the entire region. Note that for the original Hamiltonian, we have already selected the spectrum in the subspace with $\langle \sigma^z \rangle \approx 0$ [see Fig. 8(d)] to match the effective Hamiltonian that is restricted in that subspace. The nature of the manifold highlighted by the red circles is to be discussed later for Fig. 8(d). In Fig. 8(c) we show the relative error $(E_v^{\text{eff}} - E_v)/E_v$ between the exact and perturbation results, with a varying perturbation parameter g_b/Δ_b . Recall that the perturbation is valid in the dispersive regime, with $g_b/\Delta_b \ll 1$. We see that the deviation increases with g_b/Δ_b , but still remains small even for sizable g_b/Δ_b , which shows that there is actually a wide parameter region in which the perturbation theory is valid.

In Fig. 8(d) we plot the average total photon number $\sum_j \langle b_j^\dagger b_j \rangle$ and qubit excitations $\langle \sigma^z \rangle$ in both clock sectors $n_a = 0$ and 1. We can see that the nature of the pair of states previously circled in Fig. 8(c) are located in the one-photon ($\langle b_1^\dagger b_1 \rangle + \langle b_2^\dagger b_2 \rangle \approx 1$) manifold and with zero-qubit excitations $\langle \sigma^z \rangle \approx 0$. We note that the average excitation from the perturbation theory (yellow squares) is always an exact integer, while the average excitation from the exact results (blue circles) slightly deviates from integer values. This is due to the fact that, in the effective Hamiltonian of the dispersive regime, total excitations of local cavities $\sum_j b_j^\dagger b_j$ and qubit excitations σ^z are conserved separately (i.e., being good quantum numbers). However, this is a consequence of the basis change due to the Schrieffer-Wolff transformation, which effectively rotates the states into dressed basis, where the photon and qubit operators are both dressed operators: $b_j \rightarrow e^S b_j e^{-S}$, $\sigma^z \rightarrow e^S \sigma^z e^{-S}$, etc. Thus, in the original basis, there is still a small number of qubit excitations in the sector we label as $\sigma^z = 0$ in the dressed basis and similarly a small number of photons are in the sector we label as $n_a = 0$. When $g_b = 0$, the circled pairs of states in the one-photon manifold are doubly degenerate states for both $n_a = 0$ and 1 clock sectors, namely, $|0_b 1_b\rangle$ and $|1_b 0_b\rangle$. When $g_b \neq 0$, as predicted by the effective Hamiltonian [Eq. (19)], there is an effective hopping amplitude $t = (2a^\dagger a - 1)g_b^2/\Delta_b$ between neighboring local cavities, which is mediated by the intermediate qubit. The sign of the hopping amplitude changes when the clock is flipped, while the magnitude $|t| = g_b^2/\Delta_b$ should remain the same. Therefore, there should be a splitting $\delta = 2|t| = 2g_b^2/\Delta_b$ between the symmetric and antisymmetric single-particle states of the dimer, namely, $\frac{1}{2}(|0_b 1_b\rangle + |1_b 0_b\rangle)$ and $\frac{1}{2}(|0_b 1_b\rangle - |1_b 0_b\rangle)$. In Fig. 8(e) we plot the splitting in both clock sectors from the exact model, namely, $\delta_{n_a=0}$ and $\delta_{n_a=1}$ as a function of g_b/Δ_b , and compare them with the value $2g_b^2/\Delta_b$ predicted by the

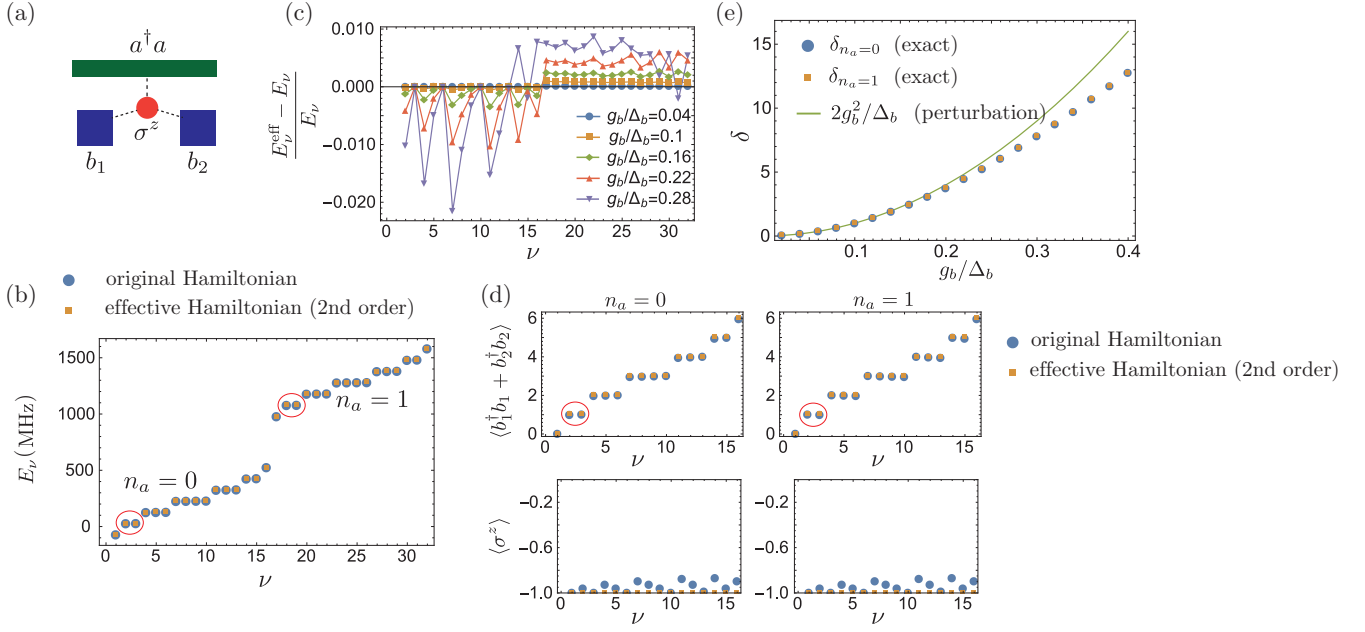


FIG. 8. Numerical comparison of the original and second-order effective Hamiltonian for a dimer. The parameters are $\Delta_b = 50$ MHz, $\Delta_a = 800$ MHz, $\chi = 50$ MHz (or equivalently $g_a = 200$ MHz), an on-site photon cutoff $n_b^{\max} = 3$. (a) The setup for numerical simulations contains two local cavities, one qubit, and one global cavity. (b) Comparison of the spectrum between the exact (blue circles) and effective (yellow squares) Hamiltonians obtained from numerical exact diagonalization. The spectrum is separated into two clock sectors. The red circle show states in the one-photon manifold ($\sum_j \langle b_j^\dagger b_j \rangle \approx 0$ and $\langle \sigma^z \rangle \approx 0$). (c) Relative error between the exact and effective spectra for $g_b/\Delta_b = 0.1$. (d) Average photon and qubit excitation numbers for the low-lying states in both clock sectors, obtained from exact (blue circles) and effective (yellow squares) Hamiltonians. The red circles show the states in the one-photon manifold. (e) Energy splitting in the one-photon manifold δ for both clock sectors obtained from exact diagonalization of the original Hamiltonian and the prediction $2g_b^2/\Delta_b$ from second-order perturbation theory.

perturbation theory. The match is very good for small g_b/Δ_b when perturbation theory is valid. In addition, we note that even when the exact result deviates from the second-order perturbation theory prediction, the splittings for both clock sectors still match. This fact suggests that our prediction of the equal magnitude of the prefactors in both clock sectors may go way beyond the second-order perturbation and may extend to all orders. In the main text we already saw this to be true for the fourth-order terms in Eq. (27) and (28), with the prefactor $(1 - 2a^\dagger a)g_b^4/\Delta_b^3$. Similarly, for k th-order perturbation, a prefactor of the form $(1 - 2a^\dagger a)g_b^k/\Delta_b^{k-1}$ is expected.

From the above verification of the dimer case, we see that there is indeed a symmetry of the magnitude of the prefactors in both clock sectors. However, we are not able to check the sign flip induced by the clock from the spectrum since the spectrum of a dimer is invariant under the sign flip of the hopping, which is equivalent to a gauge transformation. However, no gauge transformation can flip the hopping signs for a three-site periodic ring, such as the setup shown in Fig. 9(a), which is composed of three local cavities, three qubits in between, and a global ring cavity. We choose the same parameters and focus still on the one-photon manifold ($\sum_j \langle b_j^\dagger b_j \rangle \approx 1$) of the exact numerical spectrum as shown in Figs. 9(b)–9(e). We can see from the zoomed-in insets in Figs. 9(b) and 9(d) that the lowest of the three states in the $n_a = 0$ sector is singly degenerate, while in the $n_a = 1$ sector the lowest states are doubly degenerate. This can be simply understood by the formula of the effective hopping amplitude $t = (2a^\dagger a - 1)g_b^2/\Delta_b$ from Eq. (19).

For the $n_a = 0$ clock sector, the effective hopping is $t = -g_b^2/\Delta_b$, which is negative according to the current parameter choice. In this situation, the spectrum in the one-photon manifold is $\{-2|t|, |t|, |t|\}$ and the unique ground state in this manifold corresponds to the symmetric state $\frac{1}{\sqrt{3}}(|1_b 0_b 0_b\rangle + |0_b 1_b 0_b\rangle + |0_b 0_b 1_b\rangle)$. The two degenerate states with higher energy can be chosen as two counterpropagating states with opposite chirality, namely, $\frac{1}{\sqrt{3}}(|1_b 0_b 0_b\rangle + e^{\pm i 2\pi/3} |0_b 1_b 0_b\rangle + e^{\mp i 2\pi/3} |0_b 0_b 1_b\rangle)$. For the $n_a = 1$ clock sector, the effective hopping is $t = g_b^2/\Delta_b$, which is positive and hence leads to frustration of the ring. In this situation, the spectrum in the one-photon manifold is $\{-|t|, -|t|, 2|t|\}$ and the doubly degenerate ground states correspond to the two opposite chiral states, while the symmetric state has higher energy. Therefore, the signature of sign flipping is clearly shown in the two insets. In addition, for both clock sectors, the splittings ($\delta_{n_a=0}$ and $\delta_{n_a=1}$) between the lower and higher states is fixed to be $3|t| = 3g_b^2/\Delta_b$. We compare the splittings from the exact diagonalization to the prediction $3g_b^2/\Delta_b$ from perturbation theory in Fig. 9(f) as a function of g_b/Δ_b and we can see a very good match for small g_b/Δ_b . Also, the symmetry of the magnitude of the splitting in both clock sectors is again verified.

APPENDIX C: COMPLETE FORMULA OF THE SECOND-ORDER EFFECTIVE HAMILTONIAN

In the main text we derived the effective Hamiltonian of the local model constrained in the sector with zero-qubit

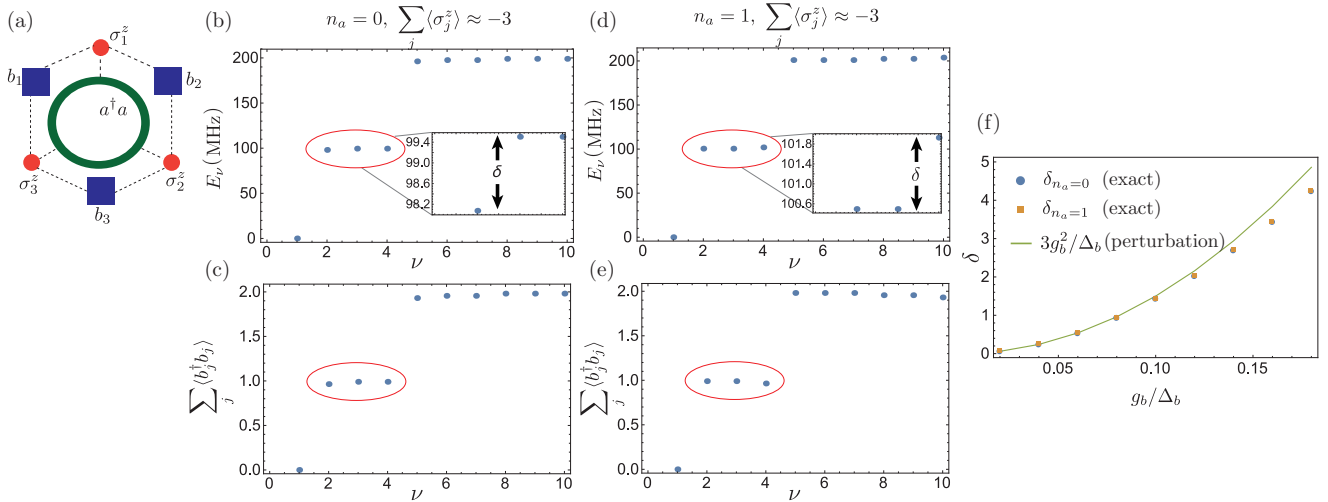


FIG. 9. Numerical results for a three-site ring. (a) The setup for numerical simulations contains three local cavities, three qubits, and one global cavity, which form a periodic ring. (b)–(e) Average photon and qubit excitation numbers for the low-lying states in both clock sectors, obtained from exact (blue circles) and effective (yellow squares) Hamiltonians. The red circles show the states in the one-photon manifold and the insets show the zoomed-in spectrum in that manifold. (f) Splitting in the one-photon manifold for both clock sectors obtained from exact diagonalization of the original Hamiltonian and the prediction $3g_b^2/\Delta_b$ from second-order perturbation theory.

excitation, i.e., $|\downarrow\downarrow\downarrow\cdots\rangle$, which corresponds to a projection $P_{S_z=0}$. Here we release such a constraint and show the full effective Hamiltonian in the dispersive regime up to second order

$$\begin{aligned}
 H_{\text{eff}} = & H_0 + \sum_{n_a} \frac{g_b^2}{\Delta_{b,n_a}} \sum_j [(b_j^\dagger b_{j+1} + \text{H.c.}) \sigma_{j,j+1}^z \\
 & + (\sigma_{j-1,j}^+ \sigma_{j,j+1}^- + \text{H.c.}) + \sigma_j^z + b_j^\dagger b_j (\sigma_{j-1,j}^z + \sigma_{j,j+1}^z)] \\
 & |n_a\rangle\langle n_a|_c + \mathcal{O}\left(\frac{g_b^4}{\Delta_{b,n_a}^3}\right). \quad (\text{C1})
 \end{aligned}$$

We see from the first term that the qubits, like a local quantum switch, mediate qubit-state-dependent hopping of photons on neighboring cavities, which has been previously explored in the context of superconducting circuits [74]. On the other hand, the second term shows the flip-flop interaction between neighboring qubits is only mediated by virtual photons (meaning there is no presence of the photon operators), i.e., the so-called quantum-bus interaction [18,54,61]. The third term represents the Lamb shift of the qubits induced by the neighboring local cavities and the last term represents the dispersive shifts (ac Stark shifts), which shows the mutual dressing of photons and qubits [18,54].

-
- [1] M. Gutzwiller, *Chaos in Classical and Quantum Mechanics* (Springer, Berlin, 1990).
- [2] S. H. Shenker and D. Stanford, *J. High Energy Phys.* **2014**, 1 (2014).
- [3] A. Kitaev, Breakthrough Prize Fundamental Physics Prize Symposium (unpublished).
- [4] J. Maldacena, S. H. Shenker, and D. Stanford, *J. High Energy Phys.* **08** (2016) 106.
- [5] A. I. Larkin and Y. N. Ovchinnikov, *Sov. Phys. JETP* **28**, 1200 (1969).
- [6] D. A. Roberts, D. Stanford, and L. Susskind, *J. High Energy Phys.* **03** (2015) 51.
- [7] D. A. Roberts and D. Stanford, *Phys. Rev. Lett.* **115**, 131603 (2015).
- [8] J. Polchinski and V. Rosenhaus, *J. High Energy Phys.* **04** (2016) 001.
- [9] J. Maldacena and D. Stanford, *Phys. Rev. D* **94**, 106002 (2016).
- [10] S. Sachdev and J. Ye, *Phys. Rev. Lett.* **70**, 3339 (1993).
- [11] S. Sachdev, *Phys. Rev. Lett.* **105**, 151602 (2010).
- [12] B. Swingle, G. Bentsen, M. Schleier-Smith, and P. Hayden, *Phys. Rev. A* **94**, 040302 (2016).
- [13] K. M. Birnbaum, A. Boca, R. Miller, A. D. Boozer, T. E. Northup, and H. J. Kimble, *Nature (London)* **436**, 87 (2005).
- [14] L. Jiang, G. K. Brennen, A. V. Gorshkov, K. Hammerer, M. Hafezi, E. Demler, M. D. Lukin, and P. Zoller, *Nat. Phys.* **4**, 482 (2008).
- [15] J. S. Douglas, H. Habibian, C. L. Hung, A. V. Gorshkov, H. J. Kimble, and D. E. Chang, *Nat. Photon.* **9**, 326 (2015).
- [16] A. G. Iez Tudela, C. L. Hung, D. E. Chang, J. I. Cirac, and H. J. Kimble, *Nat. Photon.* **9**, 1 (2015).
- [17] R. J. Schoelkopf and S. M. Girvin, *Nature (London)* **451**, 664 (2008).
- [18] A. Blais, J. Gambetta, A. Wallraff, D. I. Schuster, S. M. Girvin, M. H. Devoret, and R. J. Schoelkopf, *Phys. Rev. A* **75**, 032329 (2007).
- [19] A. A. Houck, H. E. Türeci, and J. Koch, *Nat. Phys.* **8**, 292 (2012).
- [20] J. Koch, A. A. Houck, K. Le Hur, and S. M. Girvin, *Phys. Rev. A* **82**, 043811 (2010).
- [21] A. J. Hoffman, S. J. Srinivasan, S. Schmidt, L. Spietz, J. Aumentado, H. E. Türeci, and A. A. Houck, *Phys. Rev. Lett.* **107**, 053602 (2011).

- [22] D. L. Underwood, W. E. Shanks, J. Koch, and A. A. Houck, *Phys. Rev. A* **86**, 023837 (2012).
- [23] S. Schmidt and J. Koch, *Ann. Phys. (Leipzig)* **525**, 395 (2013).
- [24] J. Raftery, D. Sadri, S. Schmidt, H. E. Türeci, and A. A. Houck, *Phys. Rev. X* **4**, 031043 (2014).
- [25] A. Chiesa, P. Santini, D. Gerace, J. Raftery, A. A. Houck, and S. Carretta, [arXiv:1504.05667](https://arxiv.org/abs/1504.05667).
- [26] S. Hacothen-Gourgy, V. V. Ramasesh, C. De Grandi, I. Siddiqi, and S. M. Girvin, *Phys. Rev. Lett.* **115**, 240501 (2015).
- [27] M. Dalmonte, S. I. Mirzaei, P. R. Muppalla, D. Marcos, P. Zoller, and G. Kirchmair, *Phys. Rev. B* **92**, 174507 (2015).
- [28] M. Fitzpatrick, N. M. Sundaresan, A. C. Y. Li, J. Koch, and A. A. Houck, [arXiv:1607.06895](https://arxiv.org/abs/1607.06895).
- [29] M. D. Lukin, *Rev. Mod. Phys.* **75**, 457 (2003).
- [30] M. Saffman, T. G. Walker, and K. Mølmer, *Rev. Mod. Phys.* **82**, 2313 (2010).
- [31] J. Ningyuan, A. Georgakopoulos, A. Ryou, N. Schine, A. Sommer, and J. Simon, *Phys. Rev. A* **93**, 041802(R) (2016).
- [32] A. Sommer, H. P. Buchler, and J. Simon, [arXiv:1506.00341](https://arxiv.org/abs/1506.00341).
- [33] K. Kim, M. S. Chang, S. Korenblit, R. Islam, E. E. Edwards, J. K. Freericks, G. D. Lin, L. M. Duan, and C. Monroe, *Nature (London)* **465**, 590 (2010).
- [34] E. T. Jaynes and F. W. Cummings, *Proc. IEEE* **51**, 89 (1963).
- [35] L. DiCarlo, J. M. Chow, J. M. Gambetta, L. S. Bishop, B. R. Johnson, D. I. Schuster, J. Majer, A. Blais, L. Frunzio, S. M. Girvin, and R. J. Schoelkopf, *Nature (London)* **460**, 240 (2009).
- [36] D. Comparat and P. Pillet, *J. Opt. Soc. Am. B* **27**, A208 (2010).
- [37] C. S. Hofmann, G. Gunter, H. Schempp, N. L. M. Müller, A. Faber, H. Busche, M. Robert-de Saint-Vincent, S. Whitlock, and M. Weidemuüller, *Front. Phys.* **9**, 571 (2013).
- [38] K. M. Maller, M. T. Lichtman, T. Xia, Y. Sun, M. J. Piotrowicz, A. W. Carr, L. Isenhower, and M. Saffman, *Phys. Rev. A* **92**, 022336 (2015).
- [39] D. Kafri and J. Taylor, [arXiv:1504.01187](https://arxiv.org/abs/1504.01187).
- [40] J. S. Pedernales, R. Di Candia, I. L. Egusquiza, J. Casanova, and E. Solano, *Phys. Rev. Lett.* **113**, 020505 (2014).
- [41] M. Müller, I. Lesanovsky, H. Weimer, H. P. Buchler, and P. Zoller, *Phys. Rev. Lett.* **102**, 170502 (2009).
- [42] M. Knap, A. Kantian, T. Giamarchi, I. Bloch, M. D. Lukin, and E. Demler, *Phys. Rev. Lett.* **111**, 147205 (2013).
- [43] D. A. Abanin and E. Demler, *Phys. Rev. Lett.* **109**, 020504 (2012).
- [44] H. Pichler, G. Zhu, A. Seif, P. Zoller, and M. Hafezi, *Phys. Rev. X* **6**, 041033 (2016).
- [45] N. Y. Yao, F. Grusdt, B. Swingle, M. D. Lukin, D. M. Stamper-Kurn, J. E. Moore, and E. A. Demler, [arXiv:1607.01801](https://arxiv.org/abs/1607.01801).
- [46] D. A. Roberts and B. Swingle, *Phys. Rev. Lett.* **117**, 091602 (2016).
- [47] P. Hosur, X. L. Qi, D. A. Roberts, and B. Yoshida, *J. High Energy Phys.* **02** (2016) 004.
- [48] Y. Huang, Y.-L. Zhang, and X. Chen, *Ann. Phys.*, doi:[10.1002/andp.201600318](https://doi.org/10.1002/andp.201600318).
- [49] R. Fan, P. Zhang, H. Shen, and H. Zhai, [arXiv:1608.01914](https://arxiv.org/abs/1608.01914).
- [50] Y. Chen, [arXiv:1608.02765](https://arxiv.org/abs/1608.02765).
- [51] B. Swingle and D. Chowdhury, [arXiv:1608.03280](https://arxiv.org/abs/1608.03280).
- [52] R. He and Z. Lu, [arXiv:1608.03586](https://arxiv.org/abs/1608.03586).
- [53] H. Shen, P. Zhang, R. Fan, and H. Zhai, [arXiv:1608.02438](https://arxiv.org/abs/1608.02438).
- [54] G. Zhu, S. Schmidt, and J. Koch, *New J. Phys.* **15**, 115002 (2013).
- [55] M. Srednicki, *J. Phys. A: Math. Gen.* **32**, 1163 (1999).
- [56] J. M. Deutsch, *Phys. Rev. A* **43**, 2046 (1991).
- [57] M. Srednicki, *Phys. Rev. E* **50**, 888 (1994).
- [58] J. Jin, D. Rossini, R. Fazio, M. Leib, and M. J. Hartmann, *Phys. Rev. Lett.* **110**, 163605 (2013).
- [59] J. Koch, T. M. Yu, J. Gambetta, A. A. Houck, D. I. Schuster, J. Majer, A. Blais, M. H. Devoret, S. M. Girvin, and R. J. Schoelkopf, *Phys. Rev. A* **76**, 042319 (2007).
- [60] S. E. Nigg, H. Paik, B. Vlastakis, G. Kirchmair, S. Shankar, L. Frunzio, M. H. Devoret, R. J. Schoelkopf, and S. M. Girvin, *Phys. Rev. Lett.* **108**, 240502 (2012).
- [61] J. Majer, J. M. Chow, J. M. Gambetta, J. Koch, B. R. Johnson, J. A. Schreier, L. Frunzio, D. I. Schuster, A. A. Houck, A. Wallraff, A. Blais, M. H. Devoret, S. M. Girvin, and R. J. Schoelkopf, *Nature (London)* **449**, 443 (2007).
- [62] J. R. Schrieffer and P. A. Wolff, *Phys. Rev.* **149**, 491 (1966).
- [63] S. Bravyi, D. P. DiVincenzo, and D. Loss, *Ann. Phys. (N.Y.)* **326**, 2793 (2011).
- [64] V. E. Manucharyan, N. A. Masluk, A. Kamal, J. Koch, L. I. Glazman, and M. H. Devoret, *Phys. Rev. B* **85**, 024521 (2012).
- [65] Y. Chen *et al.*, *Phys. Rev. Lett.* **113**, 220502 (2014).
- [66] E. H. Lieb and D. W. Robinson, *Commun. Math. Phys.* **28**, 251 (1972).
- [67] R. Barends *et al.*, *Nature (London)* **508**, 500 (2014).
- [68] V. Oganessian and D. A. Huse, *Phys. Rev. B* **75**, 155111 (2007).
- [69] M. Araujo, F. Costa, and C. Brukner, *Phys. Rev. Lett.* **113**, 250402 (2014).
- [70] V. E. Manucharyan, J. Koch, L. I. Glazman, and M. H. Devoret, *Science* **326**, 113 (2009).
- [71] G. Zhu, D. G. Ferguson, V. E. Manucharyan, and J. Koch, *Phys. Rev. B* **87**, 024510 (2013).
- [72] G. Zhu and J. Koch, *Phys. Rev. B* **87**, 144518 (2013).
- [73] N. M. Sundaresan, Y. Liu, D. Sadri, L. J. Szűcs, D. L. Underwood, M. Malekakhlagh, H. E. Türeci, and A. A. Houck, *Phys. Rev. X* **5**, 021035 (2015).
- [74] M. Mariantoni, F. Deppe, A. Marx, R. Gross, F. K. Wilhelm, and E. Solano, *Phys. Rev. B* **78**, 104508 (2008).